# Enhanced deformation of limestone and sandstone in the presence of high pCO2 fluids

Yvi Le Guen, Roland Hellmann, Marielle Collombet, Jean-Pierre Gratier,
François Renard, Etienne Brosse

## ▶ To cite this version:

## HAL Id: hal-00202346
## https://hal.science/hal-00202346

Submitted on 5 Jan 2008

# Enhanced deformation of limestone and sandstone in the presence of high $P_{CO_2}$ fluids

Yvi Le Guen,[*] Roland Hellmann,[†] Marielle Collombet,[‡] and Jean-Pierre Gratier[§]

*Laboratoire de Géophysique Interne et Tectonophysique,*
*Université Joseph Fourier, BP 53, F-38041 Grenoble, France*

François Renard[¶]

*Laboratoire de Géophysique Interne et Tectonophysique,*
*Université Joseph Fourier, BP 53, F-38041 Grenoble,*
*France & Physics of Geological Processes, University of Oslo, Norway*

Etienne Brosse[**]

*Institut Français du Pétrole, Division Géologie-Géochimie,*
*1-4 avenue de Bois Préau, 92500 Rueil-Malmaison, France*

Geological repositories subject to the injection of large amounts of anthropogenic carbon dioxide will undergo chemical and mechanical instabilities for which there are currently little experimental data. This study reports on experiments where low and high $P_{CO_2}$ (8 MPa) aqueous fluids where injected into natural rock samples. The experiments were performed in flow-through triaxial cells, where the vertical and confining stresses, temperature, and pressure and composition of the fluid were separately controlled and monitored. The axial vertical strains of two limestones and one sandstone were continuously measured during separate experiments for several months, with a strain rate resolution of $10^{-11}$ s$^{-1}$. Fluids exiting the triaxial cells where continuously collected and their compositions analysed. The high $P_{CO_2}$ fluids induced an increase in strain rates of the limestones by up to a factor of 5, compared to the low $P_{CO_2}$ fluids. Injection of high $P_{CO_2}$ fluids into the sandstone resulted in deformation rates one order of magnitude smaller than the limestones. The creep accelerating effect of high $P_{CO_2}$ fluids with respect to the limestones was mainly due to the acidification of the injected fluids, resulting in a significant increase in solubility and reaction kinetics of calcite. Compared to the limestones, the much weaker response of the sandstone was due to the much lower solubility and reactivity of quartz in high $P_{CO_2}$ fluids. In general, all samples showed a positive correlation between fluid flow rate and strain rate. X-ray tomography results revealed significant increases in porosity at the inlet portion of each core; the porosity increases were dependent on the original lithological structure and composition. The overall deformation of the samples is interpreted in terms of simultaneous dissolution reactions in pore spaces and intergranular pressure solution creep.
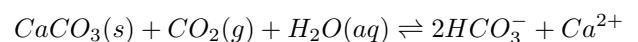
PACS numbers:

## I. INTRODUCTION

The subsurface sequestration of $CO_2$ in geological repositories is frequently cited as a promising solution for reducing the amount of anthropogenically produced $CO_2$ released to the atmosphere. Some of the major issues involved in the long-term sequestration of $CO_2$ in such sites are discussed in an overview by [62], for example. This overview considers that it is essential for models to be able to predict $CO_2$-fluid and repository behavior over periods of several thousand years. Thus, in order to advance our knowledge of the processes involved in the geological sequestration of $CO_2$, one of the most important challenges facing geoscientists is to understand and quantify all of the mechano-chemical processes, at both short and long time scales, that are relevant to $CO_2$ injection and storage in geological formations [38].

Injection of $CO_2$ into a geological reservoir has the potential of creating a chemical and flow regime disturbance that will in turn affect fluid-rock interactions, causing the porosity, permeability, and mechanical stability of the porous rock matrix to change with time. There are different reasons for this, including acidification of pore fluids by the dissociation of carbonic acid. Under the effect of high partial pressures of $CO_2$ ($P_{CO_2}$), the kinetic rates of fluid-rock interactions are potentially increased. This is particularly important in limestones, or any permeable rock that contains carbonates, where a decrease in pH (with increasing $P_{CO_2}$ in the fluid) leads to a large increase in carbonate solubility and dissolution kinetics [45].

To describe water-rock-$CO_2$ interactions in limestone, the following general chemical reaction can be used:

$$CaCO_3(s) + CO_2(g) + H_2O(aq) \rightleftharpoons 2HCO_3^- + Ca^{2+}$$

In this equation, higher $P_{CO_2}$ levels drive the calcite dis-

---

[*]Electronic address: yleguen@ujf-grenoble.fr
[†]Electronic address: roland.hellmann@ujf-grenoble.fr
[‡]Electronic address: marielle.collombet@ujf-grenoble.fr
[§]Electronic address: jean-pierre.gratier@ujf-grenoble.fr
[¶]Electronic address: francois.renard@ujf-grenoble.fr
[**]Electronic address: Etienne.Brosse@ifp.fr

solution reaction to the right and increase the concentration of dissolved calcium in the pore fluid. Thus, the porosity of the rock matrix is likely to evolve because of pore fluid acidification. On the one hand, dissolution of calcium carbonate should lead to an increase in porosity, but, in turn, the weakening of the rock limestone skeleton promotes mechanical and chemical compaction, and therefore a potential decrease in porosity. Several mechanisms can be involved in this overall process: (I) elastic strain due to a modification of the mechanical properties of the porous medium, (II) cataclastic strain, such as grain crushing, (III) compaction by subcritical crack growth [3, 41] or, (IV) compaction by pressure solution creep [17, 28, 52, 57, 63].

In the context of massive injection of $CO_2$ in aquifers, the pressure solution creep (PSC) mechanism may play a major role, particularly in carbonate rocks whose reactivity is very sensitive to the $P_{CO_2}$ of the pore fluid (note that pH decreases to a nominally stable value when $P_{CO_2}$ increases to $\approx 3$ MPa, see also results in [47]). In the presence of high $P_{CO_2}$ fluids, increased rates of dissolution (in both pore spaces and grain-grain contacts) may lead to significantly higher strain and compaction within an aquifer due to PSC. However, to the authors' knowledge, there are no data in the literature on the long-term impact of high $P_{CO_2}$ fluids on the mechanical creep of consolidated rock samples. To address this problem, we investigated the creep weakening of limestone and sandstone core samples in the presence of percolating low and high $P_{CO_2}$ fluids at conditions equivalent to a reservoir located at 800 m depth. Our experiments used specially designed triaxial cells that permitted measurement of remarkably small strain rates ($10^{-11}$ s$^{-1}$), over periods ranging from several months to two years.

As very low strain rates could be measured, our approach permitted us to investigate fluid-assisted compaction of consolidated rock samples, rather than unconsolidated granular material [10, 12, 13, 16, 17, 24, 25, 27, 51, 55, 57, 66–68]. Moreover, it allowed us to investigate compaction of a sandstone (characterized by slow compaction rates), at stress and temperature conditions corresponding to moderate depths ($< 1$ km). We thereby avoided the need to run experiments at higher temperature and stress conditions, e.g., [10, 53] to obtain measurable strain rates. Our approach permits us to directly apply our results to $CO_2$ sequestration in aquifers, and does not require extrapolation of data to environments at lower temperature and pressure conditions. The results obtained in the present study fill a gap in experimental data on long-term fluid-rock interactions, and can supplement large-scale data sets obtained from case studies where $CO_2$ has been massively injected into depleted oil reservoirs, such as Weyburn, Canada [19, 43, 48, 64], or into saline aquifers, e.g., Sleipner, Norway [2, 4, 8, 21, 34].

## II. EXPERIMENTAL METHODS AND SAMPLES

### A. Experimental set-up and rate-controlling parameters

The vertical axial strain of four core samples of porous rock (23 mm in diameter and 48 mm in height) was monitored in separate experiments for periods ranging from several months to two years, under constant load conditions, in two specially designed triaxial cells. The vertical ($\sigma_1$) and confining stresses ($\sigma_2 = \sigma_3$), fluid pressure ($P_f$), temperature, $P_{CO_2}$, and fluid flow rate were independently controlled and measured (Figure 1). The maximum values that can be achieved with these cells are: $\sigma_1 = 25$ MPa, $\sigma_2 = \sigma_3 = 13$ MPa, $P_f = 13$ MPa, T $= 150$ °C.

Experiments were performed under conventional triaxial conditions ($\sigma_1 > \sigma_2 = \sigma_3$). We assume that both volumetric and deviatoric strains occurred, but our triaxial cells only allowed the measurement of vertical axial strain (henceforth termed axial strain or axial compression). Throughout this study we refer to a quantity called the effective vertical stress, defined as:

$$\sigma_e = \sigma_1 - P_f \quad (1)$$

The vertical stress ($\sigma_1$) was imposed by a piston directly in contact with the sample. The horizontal confining stress ($\sigma_2$, $\sigma_3$) was applied via an inert gas acting over a latex sleeve enclosing the sample. This latex sleeve had a dual role: first, it transmitted the confining pressure to the sample; and second, it provided an impermeable membrane to prevent fluids from escaping. A cylindrical furnace with three heating zones ensured homogeneous heating of the sample over its entire length.

Fluids were injected by using a high pressure liquid chromatography pump (Knauer K-1001 HPLC) located at the inlet of each triaxial cell. The fluid pressure in the entire system was controlled by a back-pressure regulator located at the outlet of the triaxial cell (Figure 1). Fluid flow was from bottom to top through the sample. A perforated plate ensured an even spatial distribution of fluid at the interface between the plate and the bottom of the core. For each sample, the fluid flux remained constant, and was set at 0.005 ml.min$^{-1}$ ($8.3 \times 10^{-11}$ m$^3$.s$^{-1}$); this being equivalent to a Darcy velocity of $\sim 1 \times 10^{-6}$ m.s$^{-1}$, depending on the initial sample porosity (see Table II for details). Such low fluid fluxes are close to flow rates in natural aquifers [11]. Two different fluids were injected through the samples: moderately saline solutions ([NaCl] $= 10^{-2}$ mol.l$^{-1}$), or de-ionized $H_2O$. In both cases, fluids were unsaturated with respect to the mineral phases in the rock cores. The fluid $P_{CO_2}$ was set either equal to the atmospheric value ($10^{-4.5}$ MPa) or 8 MPa (see exact values in Table II). These fluids are henceforth referred to as 'low' and 'high' $P_{CO_2}$ fluids, respectively.

High $P_{CO_2}$ fluids were prepared in a separate 1000 ml autoclave maintained at a constant temperature (40 or

80 °C) using the following protocol. The autoclave was first filled with carbon dioxide ice and sealed. Solution was then injected until the autoclave pressure was 8 MPa. At these conditions, a supercritical $CO_2$ phase coexisted with the aqueous solution (lower density $CO_2$ located above the aqueous fluid in autoclave). Note that the critical point of pure $CO_2$ occurs at $T = 31$ °C and $P = 7.35$ MPa [58].

Rapid exchange kinetics of $CO_2$ over the interface [7], injection of solution at the top of the autoclave, and an impeller ensured an homogeneous and well-mixed solution at high $P_{CO_2}$. A tube extending almost to the bottom of the autoclave ensured that only the high $P_{CO_2}$ fluid phase was injected into the triaxial cell. After the initial preparation of the high $P_{CO_2}$ solution, new aqueous solution was continuously pumped into the autoclave, which in turn forced the existing high $P_{CO_2}$ fluid into the triaxial cell containing the rock core. This was due to the fact that the system pressure was constant and fixed at 8 MPa, set by the back pressure regulator. New fluid injected into the autoclave had ample time to equilibrate with the supercritical $CO_2$ phase, given that the residence time of more than one week greatly exceeded the kinetics of $CO_2$ exchange [7]. Moreover, the new solution injected per day represented less than 0.5% of the fluid volume in the autoclave. The composition of the $H_2O$-$CO_2$ solution inside the autoclave remained constant. To avoid any modification of the fluid composition between the autoclave and the triaxial cell, the tube linking them was heated to the same temperature as the autoclave and the triaxial cell using heating tape.

The vertical axial strain of the samples was measured with high resolution digital linear encoders (LE/12/S IP50, Solartron) at a constant time-step of 20 minutes. Two displacement sensors were installed on each triaxial cell, the first one measured the sample strain, and the second one acted as a reference, thereby ensuring that drift in the displacement sensor measurements was less than 3% of the measured strain (for the sandstone sample, as strain was exceeding small, this represented about 6%) (Figure 1). The sensitivity of the displacement sensors was 0.05 $\mu$m. When mounted on the triaxial cell, with temperature, stresses, and pressure set to experimental values, their stability over one week was less than 1 $\mu$m. This ensured a remarkably lower detection limit of $10^{-11}$ s$^{-1}$ for the strain rate. Measurement of the lateral strain was not possible in the experimental setup used.

For the samples deformed toward the end of our experimental program (Lavoux W526, W520, and the sandstone), three pressure transducers (Series 33X, Keller) were fitted to each triaxial cell. They provided an even more accurate measurement of the vertical axial stress, the confining stress, and the fluid pressure. As was the case before, displacement measurements were recorded automatically every 20 minutes. The accuracy of the transmitters was 0.002% of the measured pressure. Small variations in stresses and fluid pressure related to thermal variations in the lab could be detected with these

pressure transducers. Note, however, that when the thermal variations induced strain larger than $10^{-11}$ s$^{-1}$, the strain signal was averaged over a 24 hour period.

## B. Rock samples

To investigate the influence of mineralogy on deformation behavior, three different rock core samples were used: two limestones with different grain sizes (Estaillades and Lavoux), and one arkosic sandstone. The initial porosities and permeabilities were measured by standard techniques; the chemical compositions were determined by X-ray fluorescence (Table I).

1. The Estaillades sample is a Cretaceous bioclastic limestone, extracted from the Estaillades quarry (SE France). Optical observations of thin sections revealed it to be composed of mm-sized algae grains ($\approx$0.7-1 mm) cemented by a microsparite (Figure 2a). The initial porosity equaled 30.6%, and the permeability was 270 mD (Table I).

2. The second sample was a Dogger limestone from the Lavoux quarry (central France). It is a peloidal and bioclastic limestone (Figure 2b) with 100-200 $\mu$m-sized grains [32, 33]. Its porosity was approximately 23%, and the permeability was 12 mD. Two different core samples, with similar properties, were used: W526 and W520 (Table I).

3. The last sample was a Triassic arkosic sandstone, extracted from a bore hole in Villefranche-sur-Cher (central France). This sandstone is an assemblage of quartz ($\approx$ 73% mass) and feldspar ($\approx$ 15% mass) millimetric grains cemented with dolomite (Figure 2c). The porosity and permeability were 15.8% and 461 mD, respectively (Table I).

## C. Experimental conditions

Once the stresses and temperatures were set to the desired values, the sample was allowed to compact for several weeks in order to reach mechanical equilibrium, thereby allowing measurement of the strain rate under dry conditions. As no significant strains were measured at this stage, dry strain periods served as a reference for comparison with deformation periods in the presence of fluids. Dry deformation was followed by the injection of fluids at fixed $P_{CO_2}$ values for periods of up to several months. The experimental parameters ($\sigma_1$, $\sigma_3$, $p_f$, $T$, $P_{CO_2}$, fluid flow rate) for all samples are summarized in Table II.

### 1. Estaillades limestone

After a period of several months at dry conditions, subject to stresses of $\sigma_1 = 8.9$ MPa and $\sigma_3 = 7.9$ MPa,

two different fluids were successively injected through the sample. First, low $P_{CO_2}$ water, at ambient temperature (25 °C) was injected for 40 days. This was followed by an injection of high $P_{CO_2}$ water (7.8 MPa) at 80 °C for 6 months. During injection of water at low $P_{CO_2}$, $\sigma_1$ and $\sigma_3$ equaled 8.9 and 7.3 MPa, respectively. As a result of heating the triaxial cell and the autoclave between the two injection episodes (from 25 to 80 °C), $\sigma_1$ and $\sigma_3$ increased to 10 MPa and 8.5 MPa, respectively, during injection of water at high $P_{CO_2}$. Toward the end of the experiment, the injection was stopped and the core was allowed to deform under a no-flow regime for several weeks.

### 2. Lavoux limestone (W526)

After a period of 25 days at dry conditions, subject to stresses of $\sigma_1 = 16.3$ MPa and $\sigma_3 = 12$ MPa, a high $P_{CO_2}$ saline solution was injected through the Lavoux W526 core sample. The fluid $P_{CO_2}$ was equal to 7.9 MPa, the temperature remained constant at 40 °C during the entire experiment, and $\sigma_1$ and $\sigma_3$ were respectively equal to 16.3 and 12 MPa (Table II). The experiment using the Lavoux W526 core sample lasted 70 days. The experiment came to an abrupt end due to a malfunction that led to a sudden drop in the confining stress and finally caused sample collapse.

### 3. Lavoux limestone (W520)

After a period of 35 days at dry conditions, subject to stresses of $\sigma_1 = 16.6$ MPa and $\sigma_3 = 12$ MPa, this second Lavoux sample was subjected to two episodes of percolation of a low $P_{CO_2}$ saline fluid for more than 135 days. The fluid $P_{CO_2}$ ($10^{-4.5}$ MPa), the temperature (40 °C), $\sigma_1$ (16.3 MPa) and $\sigma_3$ (11.6 MPa) remained constant during the entire experiment (Table II). Due to a problem with a particular latex sleeve, a high $P_{CO_2}$ fluid was not injected into this core sample.

### 4. Arkosic sandstone

After a three week period at dry conditions, subject to stresses of $\sigma_1 = 16.3$ MPa and $\sigma_3 = 10.4$ MPa, a high $P_{CO_2}$ saline solution was injected into this sample, with $P_{CO_2} = 8.3$ MPa (Table II). This injection period lasted 70 days. A no-flow regime followed for 50 days. During most of the experiment $\sigma_1$ and $\sigma_3$ were equal to 16 MPa and 10.2 MPa , respectively. At the end of the experiment, $\sigma_1$, $\sigma_3$ and $p_f$ were reduced and then increased; this simulated a 100 m uplift followed by burial. The temperature was set to 40 °C for the entire experiment.

### D. Axial strain and strain rate measurements

The mechanical results presented below are given in terms of strain, $\epsilon$, and strain rate, $\dot{\epsilon}$. The strain was calculated from the axial vertical displacement measured directly on the samples:

$$\epsilon = |l - l_0| / l_0 \qquad (2)$$

where $l_0$ is the initial sample height, and $l$ is the sample height during the experiment (see inset in Figure 1). In practice, the displacement sensor directly measured the axial shortening ($[l - l_0] < 0$) of the core sample. For all samples the overall shortening after several months was less than 1%. The vertical axial creep rates (units s$^{-1}$) were calculated over periods during which all the experimental parameters (stresses, fluid pressure, fluid flow rate, $P_{CO_2}$, and temperature) were constant for more than one week:

$$\dot{\epsilon} = \frac{|l - l_0|}{l_0 . \Delta t} \qquad (3)$$

The strain rates reported in the study are 'steady-state' rates; the ad-hoc criterion for steady state we have chosen was a change in rate less than $5 \times 10^{-11}$ s$^{-1}$ during at least one week. This is justified by the resolution of the axial strain measurement.

### E. Chemical analyses

During the deformation of each sample, fluids were continuously collected at the triaxial cell outlet, and subsequently analysed by ICP-AES analysis (inductively coupled plasma - atomic emission spectroscopy, Perkin Elmer Optima 3300 DV). Fluids were sampled at ambient conditions and acidified with ultrapure $HNO_3$ to mitigate against precipitation of secondary phases. In order to collect enough fluid for ICP analysis, the concentration values for each fluid sample corresponded to about 2 days of percolation through the core.

For the Estaillades limestone and the Lavoux cores, only calcium and magnesium (dissolution of calcite and dolomite, respectively) were used to evaluate how much of the total rock (grains and cement) was dissolved and removed. For the sandstone core sample, two different calculations were performed. The first aimed to evaluate the total amount of dissolved and transported material, so we considered calcium, magnesium and silicon, assumed to be derived from calcite, dolomite, and quartz, respectively. The second calculation aimed to evaluate only the dissolution of the quartz grains and not the cement, so we only considered silicon. The calculations did not include feldspar because the aluminum concentrations were at the limit of detection.

### F. Theoretical calculations

#### 1. Injected fluid composition

In order to evaluate the chemical compositions of the injected fluids, thermodynamic calculations were performed using the geochemical speciation codes CHESS [61] and EQ3NR [65]. Both codes use the thermodynamic database SUPCRT92 [35]. Calculations using EQ3NR were based on the LLNL 'composite' (com) data base [65].

The fugacity of the $CO_2$ ($f_{CO_2}$) in the aqueous solution was determined by the fugacity coefficient of pure $CO_2$ from correlation diagrams given in [58]. Fugacity coefficients at $P_{CO_2}$ = 8 MPa ranged from $\approx$ 0.75 to 0.90, depending on the temperature. Modeling the injected solution was based on the following input parameters: composition of the solution (salinity), $f_{CO_2}$, $[H^+]$ (pH), and temperature. Activity coefficients for aqueous species were calculated (EQ3NR) using the B-dot equation. Based on theoretical calculations, the input pH ranged from 3.1 to 3.2 for the high $P_{CO_2}$ solutions, which represents a significant decrease in pH from 5.7, representative of pure water or saline solution in equilibrium with atmospheric $CO_2$ ($P_{CO_2}$ = $10^{-4.5}$ MPa).

#### 2. Degree of chemical disequilibrium

For each experimental run, the degree of chemical disequilibrium for various mineral phases, based on the Gibbs free energy of reaction, $\Delta G$, was calculated using in situ triaxial temperature, measured chemical compositions at $25\,°C$, $f_{CO_2} \approx 5.6$ MPa, and input pH (which was allowed to vary). The in situ pH at the triaxial outlet was calculated to vary between 4 and 5, reflecting consumption of $[H^+]$ during dissolution. We assumed that acidification after sampling prevented the precipitation of secondary phases which could have altered the solution composition. Free energies were calculated for the four cores, at flow and no-flow conditions. Free energy results corresponding to a flow regime were based on steady-state concentrations measured at the end of a run (or before a change to no-flow); $\Delta G$ values at no-flow conditions were based on the first fluid sample recovered after injection of fluids was restarted (i.e., expulsion of stagnant pore fluid).

### G. Tomography measurements

X-ray computed tomography (CT) was performed on the cores to investigate changes in the spatial evolution of porosity due to deformation and dissolution. The main advantage of this method is that it is non-destructive. Measurements, carried out on a medical scanner located at the Institut Français du Pétrole (IFP), involved generation of one radial slice every 1 mm along the core axes, at a pixel size resolution of 0.09 mm. CT images display attenuation represented by gray scale variations, and average porosities over each slice can then be estimated based on standard calibration techniques. CT images can also be represented by a single attenuation, corresponding to a fixed radiological density, and thereby equivalent to a fixed porosity value.

## III. STRAIN IN THE PRESENCE OF FLUIDS

### A. Instantaneous strain during initial injection of fluids into dry samples

All of the experiments started with samples in a dry 'as is' state (no additional drying procedures used). In the absence of fluid, none of the core samples showed sufficient steady-state strain to be measured accurately ($\dot{\epsilon} < 10^{-11}\text{s}^{-1}$). Immediately after the initial injection of fluid, all of the cores showed an instantaneous strain response over periods less than 1 day, followed by strain rates that steadily decreased over periods of $\approx$1 to 14 days.

This phenomenon was always observed, regardless of rock mineralogy and fluid $P_{CO_2}$. All the initial strain curves are superposed in Figure 3, with all curves having the same origin in time ($t = 0 \equiv$ start of injection). Very similar results have been reported by [28] during flow-through experiments on natural chalk samples, as well as by others with aggregates of different mineralogies [9, 14, 25, 66, 67].

### B. Steady-state creep and transient strain events

For each sample, average steady-state strain rates were estimated when all experimental control parameters were maintained fixed ($\sigma_1$, $\sigma_3$, $P_f$, fluid flow rate, fluid chemistry), and $\dot{\epsilon}$ remained constant over time periods of at least one week. An exception to this concerned the evaluation of average strain rates for the Estaillades limestone during injection of high $P_{CO_2}$ fluid- this is discussed in detail further on.

#### 1. Estaillades limestone

Average vertical axial creep rates were calculated during four successive periods of deformation: dry; water-low $P_{CO_2}$-flow; water-high $P_{CO_2}$-flow; water-high $P_{CO_2}$-no flow. Figure 4 shows the strain history for all four periods; during each period shown the experimental parameters remained constant. Average strain rates are indicated directly in Figure 4.

During the initial phase of deformation under dry conditions, no significant strain was measured (Figure 4, magenta curve), and the average strain rate was at the detection limit ($\leq 10^{-11}$ s$^{-1}$). After injection of the low

$P_{CO_2}$ fluid started, the strain rate immediately increased, resulting in an average strain rate of $\dot{\epsilon} = 1.9 \times 10^{-11}$ s$^{-1}$ (Figure 4, green curve and Table III). The strain and strain rate significantly increased with injection of the high $P_{CO_2}$ water, as shown in Figure 4 (blue and black curves). The average strain rate was $\dot{\epsilon} = 3.3 \times 10^{-10}$ s$^{-1}$, which is approximately one order of magnitude higher than the low $P_{CO_2}$ average strain rate. A detailed examination of the deformation behavior for the period 344 to 370 days (Figure 4, blue curve) reveals a 'staircase' pattern characterized by a series of steady-state strain rates (flat, plateau-like periods) alternating with abrupt increases in the strain rate. The strain rate plateaus typically have $\dot{\epsilon}$ values ranging from $\approx 1.0$ to $1.5 \times 10^{-10}$ s$^{-1}$, whereas the abrupt transient events have strain rates on the order of $\approx 5 \times 10^{-10}$ to $5 \times 10^{-8}$ s$^{-1}$.

Further on in time, but with no changes in experimental parameters, the interaction between the injected high $P_{CO_2}$ water and the Estaillades sample led to much greater strain and an order of magnitude higher average strain rate, $\dot{\epsilon} = 2.2 \times 10^{-9}$ s$^{-1}$ (Figure 4, black curve). During this time period the 'staircase' deformation behavior was even more pronounced. Plateau regions typically had strain rates ranging from 0 to $\approx 1 \times 10^{-10}$ s$^{-1}$. Most of these plateau rates were of the same magnitude as those earlier in time at high $P_{CO_2}$ (Figure 4, blue curve), but an order of magnitude greater than the average strain rate at low $P_{CO_2}$ conditions ($\dot{\epsilon} = 1.9 \times 10^{-11}$ s$^{-1}$). One very large transient strain event occurred at 450 to 454 days; the change in strain was $\Delta\epsilon = 3.5 \times 10^{-3}$ and the strain rate was $\dot{\epsilon} = 1.1 \times 10^{-8}$ s$^{-1}$. This strain far exceeded all other events, such that its contribution to the global strain was approximately 74%. It is interesting to note that over the period 345 to 459 days, several strain vs. time segments had a positive slope, i.e, negative strain rate. The exact reason for this is unknown; it may represent a response to the sudden transient collapse events that preceded them.

The aforementioned 'staircase' deformation behavior was only noted in the presence of high $P_{CO_2}$ fluids, for both the Estaillades limestone and the sandstone (discussed later), and possibly also the Lavoux W526 limestone. These sudden, transient high strain rate events occurred for periods ranging from several hours to several days, and the measured strain rates varied by several orders of magnitude. These characteristics would seem to indicate that these strain events were caused by high dissolution rates producing some kind of mechanical collapse of the rock matrix, and not due to stick-slip behavior of the Viton piston o-rings with the internal wall of the triaxial cell (Figure 1).

The last period, starting at 475 days, was based on deformation in the presence of high $P_{CO_2}$ water, but with no flow. The average strain rate was $3.0 \times 10^{-11}$ s$^{-1}$ (Figure 4, red curve), which represented a decrease by a factor of 10 compared to many of the plateau strain rates measured during injection of the high $P_{CO_2}$ water.

### 2. Lavoux limestone (W526)

The experiment started under dry conditions (Figure 5). An axial creep rate at the detection limit was initially measured during this period. Injection of high $P_{CO_2}$ saline solution started on day 95 (Figure 5). Injection was interrupted over two time periods: 113-128 and 140-173 days. The measured average strain rate for the period 120-173 days was $1.0 \times 10^{-10}$ s$^{-1}$ (note that this average $\dot{\epsilon}$ included a 12-day flow period, but this did not apparently have an important effect on the overall $\dot{\epsilon}$, see Figure 5 and Table III).

From day 173 to the end of the experiment, high $P_{CO_2}$ saline solution was once again injected at the same rate as earlier. The rate of deformation did not immediately increase; however, a sharp increase in strain rate occurred at 210 days, about 40 days after injection was restarted. The exact reason for the time lag is not known. The average strain rate measured from 173-210 days was $8.8 \times 10^{-11}$ s$^{-1}$, whereas at time greater than 210 days the strain rate increased to $4.5 \times 10^{-10}$ s$^{-1}$ (Figure 5 and Table III). The Lavoux sample did not display the deformation behavior evidenced for the Estaillades limestone, with the possible exception at the very end of the experiment. Here, there was evidence for long-term steady-state strain rate behavior that was suddenly replaced by a sharp increase in the deformation rate ($\dot{\epsilon} = 2.1 \times 10^{-9}$ s$^{-1}$), followed by a plateau with a strain rate below the detection limit over the last three days of the experiment.

### 3. Lavoux limestone (W520)

Stabilization under stress and in the absence of fluid (strain at detection limit of sensors) was carried out over the first 42 days (Figure 6). This was followed by the injection of low $P_{CO_2}$ saline solution, causing an immediate deformation of the sample. The initial strain rate was $1.5 \times 10^{-9}$ s$^{-1}$ over the time period of 49 to 54 days. The strain rate decreased steadily with time, evolving to $5.6 \times 10^{-10}$ s$^{-1}$ over the period 92-125 days. At 125 days, the injection was stopped, but the strain rate remained nearly unchanged. The strain plateau between days 168 and 180 is an artifact due to the lack of data. After a time lag of 75 days, the deformation behavior showed an unmistakable and long-term decrease in the steady-state strain rate ($\dot{\epsilon} = 8.1 \times 10^{-11}$ s$^{-1}$). Injection of the same saline solution occurred at 228 days, this causing an immediate increase in the average steady-state strain rate ($2.6 \times 10^{-10}$ s$^{-1}$, Figure 6 and Table III).

### 4. Arkosic sandstone

Figure 7 shows the strain history of the arkose sandstone sample. Measured strains at dry conditions were close to the resolution of the displacement sensors. The

sample remained in a stressed state with no fluid until day 59, at which point injection of the high $P_{CO_2}$ saline solution started; injection continued until day 133. Over the first few days of saline injection, the sample rapidly deformed (see Fig. 3). Thereafter, the sandstone deformed at a much slower rate, with the rate eventually becoming non-measurable. Over the period 133-222 days, solution injection was stopped. Two sudden transient strain events occurred at days 161 and 162 (average $\dot{\epsilon} = 2.7 \times 10^{-8}$ s$^{-1}$), with overall behavior very similar to that measured for the Estaillades limestone. Moreover, the magnitude of two strains was equivalent to the smallest strain events for the Estaillades limestone. During the no-flow period, the strain rate was below $10^{-11}$ s$^{-1}$, excluding the two transient strain events just discussed. In order to simulate an uplift/burial event, the vertical and confining stresses were decreased by 2.1 and 1.1 MPa, respectively, on day 187, and then subsequently increased by 2.1 and 2.5 MPa on day 215. Core elastic dilation and compaction were measured as a consequence of the two stress changes. After day 222, an injection period using the same fluid and lasting for 33 days was started. During the first 12 days, fluids were injected at a rate 10 times greater than the initial flow rate, and for the remaining period the flow rate was twice the initial rate. During these periods, the strain rate was constant within measurable resolution. The higher compaction rate at the end of the experiment was due to a decrease in the confining stress.

## C. Effect of $P_{CO_2}$ on fluid chemistry

The pH of the high $P_{CO_2}$ solutions was significantly lower than the low $P_{CO_2}$ solutions (3.1 vs. 5.7), and this of course had a major influence on the interactions of the solutions with the samples, and in particular with respect to the limestones. Considering only the effect of pH decrease on calcite dissolution kinetics, [6] showed that the rate of dissolution increases by almost 1.5 orders of magnitude when pH is decreased from 5.7 to 3.1. Calcite solubility is also 80 times greater at $P_{CO_2} = 8.0$ MPa than at atmospheric $P_{CO_2}$ (calculations made with CHESS [61]). In the present study, the chemical composition of the fluids measured at the triaxial cell outlet changed significantly as a function of $P_{CO_2}$. Results of the chemical analyses are presented in Figure 8.

### 1. Estaillades limestone

Figure 8a shows the smooth evolution of the concentrations of several species in the presence low $P_{CO_2}$ water at 25 °C over the time period 180-220 days. Injection of high $P_{CO_2}$ had the effect of significantly increasing the concentrations of most elements (except Si). The overall increase in elemental concentrations is due to both a decrease in pH and an increase in temperature; both

of these factors increase the dissolution kinetics of all the mineral phases constituting the sample, except for quartz (the dissolution kinetics of quartz at fixed temperature are relatively invariant over the pH range 2-5 [5, 36]). Calcium and magnesium concentrations increased by 1.5 to 2 orders of magnitude, respectively. The higher variability in the chemical composition trends is due to irregular flow rates at 80 °C.

### 2. Lavoux limestone (W520)

Figure 8b shows that the concentrations underwent a smooth monotonic decrease before becoming relatively constant after about 60 days of sampling. Following the 90-day period at no-flow conditions, the re-initiation of injection expulsed the stagnant pore fluids, resulting in pronounced concentration spikes of all elements, except Na which displayed conservative behavior (present in input solution). The concentrations of Ca and Mg evolved to final, stable concentrations that were slightly lower than those just prior to when injection was stopped.

### 3. Lavoux limestone (W526)

Compared to the injection of the low $P_{CO_2}$ fluid through the W520 Lavoux limestone, the injection of the higher $P_{CO_2}$ saline solution into the Lavoux W526 core at the same temperature resulted in increases (up to 1 order of magnitude) in the concentrations of all elements (Figure 8c). Overall, the concentrations showed relatively smooth, monotonic decreases with time.

### 4. Arkosic sandstone

During the first period of high $P_{CO_2}$ saline fluid injection, the injection rate was the same as during the other experiments (0.005 ml.min$^{-1}$). All concentrations (except Mg) decreased with time (Figure 8d) up until the injection was stopped. Re-initiation of injection resulted in the expulsion of stagnant pore fluid in the core, resulting in highly elevated, but transient, concentrations. The second injection period was characterized by two flow rate regimes, the first 10x higher and the second 2x higher than the initial injection rate. In general, the steady-state concentrations decreased as a function of the flow rate increase (1x $\rightarrow$ 10x), and then increased in a step-like manner with the subsequent decrease in injection rate (10x $\rightarrow$ 2x). During the initial flow period and then the 10x flow period, the absolute Ca concentrations may be artificially too low, due to a filtration step before acidification, which may explain the divergence of the Ca and Mg concentrations. The overall higher concentrations of Ca and Mg vs. Si reflects the greater reactivity of the dolomite and calcite cement compared to the quartz grains.

## D. Porosity variations based on X-ray tomography and chemistry

### 1. Estaillades limestone

After slightly more than 600 days of deformation in the presence of both low and high $P_{CO_2}$ water, there is indirect evidence that the inlet and outlet regions of the core became more porous, by up to a few percent. Unfortunately, no X-ray computerized tomography (CT) images were taken of the core before deformation (Figure 9). However, two other undeformed Estaillades limestone cores were analysed. Taken together, the results show elevated heterogeneity in the undeformed state. Nonetheless, using CT-based porosity profiles, the deformed sample displays higher porosity both at the inlet and outlet regions compared to the two undeformed samples (Figure 9a). Figures 9b & c show CT images of two different cores, the first undeformed, the second deformed (note that former and the latter cores are not the same). The CT image of the core in Figure 9b (whose porosity profile EstG-02 is shown in Figure 9a) was chosen for comparison based on its global porosity being very similar to the central porosity of the deformed core shown in Figure 9a. As was the case for the porosity profiles (Figure 9a), a direct quantitative comparison is not possible between the CT images in Figures 9b & c. However, Figure 9c does show increased porosity in the inlet and outlet regions, which is compatible with the porosity profile after deformation in Figure 9a. Over the first third of the core sample the porosity increase is not uniformly distributed, but rather localized along preferential paths. These paths appear to be larger close to the inlet and get thinner downstream along the core axis. Three radial CT density slices are also presented in Figure 9c. The dark areas are low density, porous regions that represent preferential dissolution and fluid flow paths. Their positions within the core are shown directly in Figure 9c.

Using mass relationships and the total amount of Ca and Mg measured in the aqueous samples, the total volume of material (calcite and dolomite) dissolved and transported out of the core was $\approx 469$ mm$^3$, which corresponds to a 1.9% overall increase in porosity. This is compatible with the porosity increases in the profile shown in Figure 9a.

### 2. Lavoux limestones

Figures 9d & e show CT images (attenuation 1965) before and after deformation. Even though the W520 sample suffered shear failure at the end at the experiment, it is still possible to ascertain an increase in porosity due to dissolution and deformation in the presence of the low $P_{CO_2}$ fluid. The increase in porosity was most pronounced along the core axis, and extended almost uniformly from inlet to outlet. This can be interpreted to indicate dissolution and material transport were more im-

portant along the central axial zone.

Based on aqueous Ca and Mg (Si had a negligible contribution), the total volume of material (calcite and dolomite) lost was 33.2 mm$^3$, corresponding to a porosity increase of 0.2%. The W526 sample, subject to high $P_{CO_2}$ fluid percolation, lost significantly more material, 204.4 mm$^3$, which is equivalent to a 1.1% increase in porosity. The order of magnitude difference is due to the higher rate of dissolution and elevated solubility of the carbonates in the presence of the high $P_{CO_2}$ fluid.

### 3. Sandstone

Although the same sandstone core was imaged by X-ray tomography before and after deformation, the CT density levels for this sandstone were not calibrated, and thus it was not possible to quantify the porosity differences due to deformation that are shown in Figure 9f. The initial porosity value ($\approx 15.8\%$) was determined by an independent method. Nonetheless, the CT scans before (Figure 9g) and after deformation (Figure 9h) show that dissolution resulted in a real, but not quantifiable, increase in overall porosity. The greatest increase was concentrated in the inlet region, and decreased toward the central region. Whether the modest difference in porosity from the central region to the outlet is real or not is difficult to evaluate (Figures 9f, g & h). The radial CT slices show that distinct channelization did not occur because dissolution was probably spatially more homogeneous (dissolution of uniformly distributed cement, Figure 9h). This is in contrast to the channelization that occurred in the Estaillades limestone, as shown by the strong porosity contrasts within the CT slices in Figure 9c.

Based on the total amount of dolomite and calcite removed (present as cement), the volume of material dissolved and removed was estimated to be 358 mm$^3$, corresponding to a global increase in porosity of 1.7%. If only Si removal from the quartz grains is considered (27 mm$^3$), then the porosity increase is significantly less, 0.1%.

## IV. DISCUSSION

### A. Instantaneous strain induced by initial fluid injection

Three observations stand out, as shown in Fig. 3: a) all samples showed an extremely rapid compaction response ($\leq 1$ day); b) fluid composition (high vs. low $P_{CO_2}$) did not have an apparent influence on compaction of the two Lavoux cores; c) the sandstone and the Estaillades limestone had the same amount of total strain after the first day of compaction, despite differences in vertical stress and mineralogy. If it is assumed that injection caused rapid ($\leq 1$ day) fluid-saturation of the cores, then this would have led to a concomitant and sudden increase in

pore fluid pressure. Pore pressure effects probably facilitated rapid compaction by way of mechanical lubrication processes, such as grain-grain rearrangement and grain-grain sliding. Moreover, it is probable that this same phenomenon caused the sudden compaction event ($\approx 1$ day duration) that can be evidenced in the sandstone strain curve at time 13.5 days (Fig. 3). Thus, it is reasonable to suppose that injection of fluids caused rapid deformation primarily via a pore pressure-mechanical effect.

Nonetheless, as discussed further on, the contribution of chemical reactions cannot be discounted. A common method to discriminate between mechanical and chemical effects is the injection of a non-solvent (non-polar) fluid. Such an experiment was not carried out in the present study; however, this has been investigated in other studies. In a study of granular calcite compaction by [67] it was shown that fluid-assisted initial compaction by non-solvent fluids was only measurable when the preceding dry compaction step occurred at less than 8 MPa; above this value grain matrices became locked up and were not susceptible to fluid-assisted deformation by non-solvent fluids. However, even locked up matrices compacted rapidly during the injection of solvent fluids, showing that chemical reactions involving calcite can also induce rapid deformation.

The results in the present study, which show initial rapid compaction without an important dependence on fluid chemistry ($P_{CO_2}$ and pH), presumably demonstrate that the preceding dry compaction steps did not completely lock up the grain matrices of the rock cores, and thus fluid injection induced compaction predominantly via a mechanical effect. However, given that the injected fluids were completely unsaturated with respect to the mineral phases of all cores, chemical reactions (especially for the limestones) most probably played an important but secondary role, especially at the inlet region of each core.

Another important parameter was the effective vertical stress, as it is positively correlated with the total strains measured over the period of 0 to 14 days for all samples. On the other hand, the sandstone and the Estaillades limestone, subjected to different effective vertical stresses, had the same total amount of total strain over the first few days (0-6 day). Whether the subsequent divergence (6-14 day) in the two respective strain curves was due to mineralogy or the difference in effective stresses could not be ascertained. Part of the answer may lie with the effects of other parameters, such as temperature, initial porosity, grain size, and internal structure; however, unraveling the roles for all of these individual parameters was not possible.

## B. Long-term strain behavior

In the present study, after a period of instantaneous strain due to the initial injection of fluids, all samples displayed a global deformation behavior characterized by continuous deformation that was controlled by various rate-influencing experimental parameters discussed below.

### 1. Vertical effective stress

As was the case for the amplitude of the initial strain, the effective vertical stress was one of the primary rate-determining parameters for long-term deformation. The diagram in Figure 10a shows 3 sets of data: a) flow regime with low $P_{CO_2}$ fluids: Estaillades ($t = 198\text{-}221$ d, 25 °C) and Lavoux W520 ($t = 231\text{-}282$ d, 40 °C) b) flow regime with high $P_{CO_2}$ fluids: Estaillades ($t = 366\text{-}370$ d, 80 °C) and Lavoux W526 ($t = 209\text{-}258$ d, 40 °C) c) no-flow regime with high $P_{CO_2}$ fluids: Estaillades ($t = 475\text{-}495$ d, 80 °C) and Lavoux W526 ($t = 120\text{-}175$ d, 40 °C). The strain-time data used to determine strain rates represent the most stable and slowest evolving part of each relevant data set. It should be noted that the strain rate vs. vertical effective stress relations in Figure 10a should be interpreted with caution because various parameters (temperature, saline vs. water fluid composition, strain) were not the same in the Estaillades and Lavoux experiments. However, as shown further on, this did not have an important effect on the strain rate-effective stress relation.

The strain rate-effective stress relations in Figure 10a (log-log space) revealed that 2 of the data sets have slopes of 1.1 and 0.9 (high $P_{CO_2}$), and the third set yielded a slope of 2.5 (low $P_{CO_2}$). Slopes with a range of 1 to 3 typify most fluid-assisted deformation experiments at moderate effective stresses [12, 13, 17, 27, 28, 57].

Based on theoretical approaches and empirical relations reported in previous studies [17, 44, 56], the dependence of the compaction creep rate on the effective normal stress may be expressed as $\dot{\epsilon} \propto \sigma_e^n$, where $\dot{\epsilon}$ is the strain rate, $\sigma_e$ is the effective normal stress, and $n$ is an exponent. The value of $n$ depends on the limiting process, with $n$ taking values of 1 to 3 for dissolution or precipitation, and $n \approx 1$ for diffusion [15, 44].

### 2. Mineralogy

The relation between mineral composition and deformation rates is often expressed in terms of either mineral solubility or reaction kinetics. Taking the first case, one can write a constitutive relation based on $\dot{\epsilon} \propto C^{eq}$ if diffusion is the limiting parameter; $C^{eq}$ is the equilibrium concentration (at $T, P$ of interest) of a given element in the pore fluid derived from dissolution of a specific mineral. Alternatively, if $\dot{\epsilon} \propto k$ a chemical reaction (dissolution, precipitation) is rate-limiting; in this case $k$ is a kinetic rate constant (dissolution in intergranular contact zone, precipitation in pore volume).

Since we could not distinguish between the two limiting cases, we simply show in Figure 10b the positive correlation between (log) strain rate and (log) mineral solubility. The mineral solubilities were based on $[Ca]$ for the limestones and $[Si]$ for the sandstone as a function of temperature, pH ($P_{CO_2}$), and fluid composition (saline vs. water) at the inlet of the triaxial cell, calculated with the code CHESS [61]. The slopes for the flow regime and the no-flow regime data are 0.3 and 0.4, respectively. The dispersion of the data in the no-flow regime for the limestones is quite high, due in particular to a very low strain rate measured for the Estaillades limestone at low $P_{CO_2}$. The positive relation between the strain and strain rate as a function of mineral solubility has also been corroborated by other experimental studies [14, 53].

### 3. Internal structure

The aqueous chemistry results point to the importance of the internal lithological structure and how it affects deformation behavior. As an example, the total volume of calcite and dolomite dissolved and removed from the sandstone core (358 mm$^3$) was approximately equivalent to that of the Estaillades core (469 mm$^3$), and yet the total strain of the sandstone was an order of magnitude less than that of the Estaillades sample. In both cases deformation occurred in the presence of high $P_{CO_2}$ fluids, and in addition, the effective vertical stress imposed on the sandstone ($\sigma_e = 7.7$ MPa) was more than twice that imposed on the Estaillades limestone ($\sigma_e = 3.0$ MPa). This seemingly contradictory data can be explained by the fact that the sandstone is composed of quartz grains that are cemented by dolomite and calcite, and that the cement was preferentially removed by dissolution, as shown by [Mg, Ca] $>>$ [Si] (Figure 8). The volume of dissolved quartz only represented a porosity increase of 0.1%. Apparently dissolution left behind a quartz grain skeleton that, despite having lost some cement, remained strong enough to resist deformation. In contrast, as calcite grains supported the stress in the limestone core samples, the dissolution of grains had a much greater effect on the magnitude of the strain and strain rate.

This observation from the present study is consistent with batch experiments on an arkosic sandstone in the presence of brine under $P_{CO_2} \approx 4.8$ MPa at 40 °C [37]. These authors concluded that the initial impact of $CO_2$ injection was the dissolution of the carbonate cement, and can be explained by the large difference in dissolution rates between calcite and quartz: $k_{qtz} << k_{calc.}$. The effect of a resistant granular skeleton has also been documented by [68].

### 4. Fluid flow rate

Fluid flow rate had a direct influence on deformation rate. This was especially noticeable for the Estaillades and Lavoux limestones (see Figures 4, 5, 6 and Table III). The overall influence of flow rate on strain rates for all of the samples in the present study is shown in Figure 10b. In this diagram each individual strain rate measured at flow conditions always exceeded the corresponding strain rate at no-flow conditions (i.e., see vertically-paired data points, Figure 10b).

The mechanism that explains how flow rate influences fluid-assisted deformation is based on the fluid saturation state in the pore fluid. Compared to a flow regime, under no-flow conditions, pore fluids become chemically saturated with respect to the mineral phases present (dependent on kinetics). This has two consequences: i) it decreases or even stops the kinetics of free face dissolution; ii) it decreases the diffusion gradient between the intergranular fluid and the pore fluid, thereby decreasing the rate of mass removal (i.e., via the thin fluid film mechanism). Chemical saturation in pore spaces can be expressed in terms of $\Delta G$ for various mineral phases (see review in [26]).

The coupling between $\Delta G$, flow rate, and strain rate was observed for the limestones and the sandstone in the present study, and is apparent in Figure 10b. Values for $\Delta G$ for major mineral phases are given in Table IV. $\Delta G$ values at flow conditions were based on the steady-state fluid concentrations that corresponded in time to the relevant strain rate measurements. At no-flow conditions, $\Delta G$ values were calculated based on the concentration spikes recorded in the first sample collected after resumption of fluid injection.

In Figure 10c, the inverse relation between strain rates and $\Delta G_{calcite}$ for the limestone and $\Delta G_{quartz}$ for the sandstone experiments shows how increasing pore fluid saturation (i.e., increasing $\Delta G$) is coupled to decreasing strain rates. This diagram is based on flow/no-flow strain rate data pairs for each sample at low and high $P_{CO_2}$. The strain rates shown are the same as those used in Figure 10a & b. Note the similarity in the slopes, independent of mineralogy.

The results in the present study on fluid flow are in agreement with experiments of [25] on quartz aggregates at 34.5 MPa effective stress and 150 °C, at different fluid flow conditions. Fluid flow was found to increase strain rates by a factor 2 to 7, compared to strain rates in closed systems (zero flow rate). At similar conditions and with the same samples, [9] measured strain rates about two times higher than at no-flow conditions. On gypsum aggregates, [13] measured 10 to 30-fold faster compaction rates in open-system compared to closed-system conditions.

*5. Fluid* $P_{CO_2}$

Long-term deformation rates of the Estaillades and Lavoux limestone were significantly increased when high $P_{CO_2}$ fluids where injected. A comparison of low vs. high $P_{CO_2}$ fluids on the rate of sandstone deformation could not be evaluated, given that only a high $P_{CO_2}$ fluid was injected. However, it can be estimated that it would have deformed slower in a low $P_{CO_2}$ fluid, based on a decrease in the reactivity of the carbonate cement that binds together the quartz grains. The effect of high $P_{CO_2}$ is predominantly related to the pH: low $P_{CO_2}$ water and saline solution have a pH of 5.6-5.7, the pH decreases to 3.1-3.2 at high $P_{CO_2}$. The decrease in pH directly increases the rate of dissolution [6], as well as the solubility of calcite (CHESS, [61]).

The differences in strain rates of the Estaillades limestone in the presence of low $P_{CO_2}$ and high $P_{CO_2}$ water (flow regime) varied from 1 to 2 orders of magnitude (see Figure 4 and Table III). This comparison includes the effect of the sudden transient strain events (Figure 4, black curve). The Lavoux limestone also deformed significantly faster in the presence of the high $P_{CO_2}$ saline solution (see figure 5, 6 and Table III), but the difference (less than an order of magnitude) was markedly less than for the Estaillades limestone. This may be a consequence of its internal lithological structure and grain size distribution.

As can be seen in Figure 8, $P_{CO_2}$ levels greatly influenced the amount of material dissolved and removed from the limestone, in particular with respect to Ca and Mg. Figure 10d shows the positive correlation between the strain rates and calcium concentration for 3 data sets: Estaillades (low and high $P_{CO_2}$, flow); Lavoux (low and high $P_{CO_2}$, flow); Lavoux (low and high $P_{CO_2}$, no-flow). The strain rates shown are the same as those used in Figure 10a, b & c; [Ca] were based on the steady-state fluid concentrations that corresponded in time to the relevant strain rate measurements. At no-flow conditions, [Ca] were based on the concentration spikes recorded by the first sample collected after resumption of fluid injection (as in Figure 10c). It is interesting to note that elements such as Si, derived primarily from quartz dissolution, did not show a direct dependence on $P_{CO_2}$. This follows as a consequence of quartz dissolution kinetics that are relatively constant in the pH range of 2-5 [5, 36].

A direct comparison with other experimental studies was not possible since, to the best of our knowledge, this is the first study to report deformation rates as a function of $P_{CO_2}$. However, one theoretical study in particular examined the relation between fluid $P_{CO_2}$, pH, and carbonate deformation rates [52]. Therein it was shown that at high $P_{CO_2}$ (up to 30 MPa), carbonate compaction rates can be increased by a factor 50 to 75 times, this also causing a decrease in rock matrix viscosity.

## C. Porosity variation - X-ray tomography

Figures 9a-h show that porosity evolved during deformation for all samples, resulting in a generalized increase in porosity, to a maximum of 1-2% in the inlet region. Depending on the sample, the elevated porosity zones had a conical geometry, being most pronounced at the inlet regions and tapering off along the axis to the central portion of the cores. The creation of porosity at the inlet is an expected result, given that the injected solutions were completely undersaturated at the inlet (very low $\Delta G$), and therefore the dissolution rates were highest. As the fluids percolated through the samples, the concentrations of dissolved material increased, leading to an increase in saturation of the pore fluids (i.e. increase in $\Delta G$) and a concomitant decrease in dissolution and diffusion rates. The pH of the fluids increased as a function of percolation length, as well.

Comparisons with a study of chalk deformation and porosity development by [29] can be made. That study was based on detailed porosity measurements before and after deformation, made in conjunction with X-ray CT images. Although global porosity decreased from inlet to outlet, the porosity evolution of the chalk was spatially very heterogeneous. This was also revealed by CT scans that showed wormholes and other similar dissolution-porosity features that were evidence for preferential fluid flow (compare to CT slices in Figure 9c in present study). A recent study by [23], using similar Lavoux limestone samples, but not subjected to stress, showed that porosity increases were greater close to the fluid inlet and along preferential paths within the cores. However, it appears that the paths of greater porosity were thinner and penetrated further into the core sample.

The significance of the high porosity zones in the present study with respect to deformation can be qualitatively estimated. If enhanced dissolution was responsible for the creation of elevated porosity regions (localized at the inlet and extending to the central part of each core), then those areas should have been zones where most of the strain was localized. It is reasonable to postulate that the sudden transient strain events, especially those that characterize the high $P_{CO_2}$ deformation of the Estaillades sample (Figure 4), preferentially occurred in the elevated porosity zones due to a general fragilization of the rock matrix by rapid dissolution reactions at low pH (pH $= 3.1 - 3.2$). Moreover, given that fluid saturation increased along the core axes, it is likely that any precipitation of secondary phases within the pore spaces should have occurred within the outlet regions; this may have served to mechanically stabilize the matrix.

### D. Deformation mechanisms

#### 1. Mechanical grain interactions

Considered first is grain cataclasis, which may occur during the dry stress loading of the sample (especially when the piston is seated on the core), and may account for an important part of the recorded dry deformation. However, once steady-state dry deformation was attained (i.e. $\dot{\epsilon} \approx 0$), the effective stresses were too low for cataclasis to have occurred on a large scale throughout the sample. Small scale cataclasis, as a part of a pressure solution mechanism, may have been operative, and is discussed further on. The initial injection of fluids is postulated to have led to deformation by another type of mechanical interaction: grain-grain sliding and grain-grain rearrangement.

#### 2. Elastic and plastic strain

To evaluate the importance of elastic strain with respect to the total strains measured in the present study, we used Luo and Weng's homogenization method [42]. This method was used to determine whether the displacement measured on the Estaillades core sample could be accounted for by a modification of its elastic properties (bulk modulus) due to an increase in porosity. The Estaillades limestone can be considered to be a two phase rock: a solid phase (69.4%, almost pure calcite) and a fluid phase (pore spaces filled with water). The Luo and Weng method allows the determination of the effective Young's modulus and effective Poisson's ratio, based on the mechanical properties of the two phases and their volume distribution. At the end of the experiment, based on the aqueous chemistry data, the overall porosity increased by about 1.9%, this corresponding to a maximum decrease in the bulk modulus of 10% (with an initial value of $K_0 = 3.3$ GPa). The elastic vertical strain related to a variation of bulk modulus is equal to:

$$\Delta\epsilon_a = \frac{1}{1+2\nu}\frac{\sigma_{mean}(K_{0_{final}} - K_{0_{initial}})}{K_{0_{final}}K_{0_{initial}}} \qquad (4)$$

where $\epsilon_a$ is the axial strain, $\sigma_{mean}$ is the mean stress applied to the sample, defined as $(\sigma_1 + \sigma_2 + \sigma_3)/3$, $\nu$ is the Poisson coefficient, and $K_0$ is the bulk modulus. Hence, with constant vertical and horizontal stresses equal to 10.0 MPa and 8.5 MPa, respectively (in presence of high $P_{CO_2}$ fluids), the theoretical vertical axial strain is estimated to equal $1.7 \times 10^{-4}$. This value for the strain induced by a change in the elastic properties of the rock is one order of magnitude lower than the strain measured experimentally. Thus, while the elastic strain cannot be completely neglected, it cannot be considered to be a major deformation mechanism in the present study.

At conditions in the upper crust ($< 5$ km) the effective stresses and temperatures are far too low for pervasive intercrystalline plastic deformation to occur in clastic rocks and carbonates [46], and thus this mechanism can also be discounted with respect to the present study. However, there is a possible role for plastic deformation occurring on a micro-scale at individual grain-grain boundaries, based on some of the PSC mechanisms discussed further on.

#### 3. Subcritical crack growth

Another possible mechanism that may have been important during our experiments is subcritical crack growth, induced by a stress-corrosion process. Subcritical crack growth is a mechanism whereby rocks, subject to a constant stress (inferior to failure strength), undergo a permanent, time-dependent deformation, especially in the presence of aqueous fluids [41]. Based on the results presented here, we cannot rule out a possible contribution by subcritical crack growth to the measured time-dependent compaction. However, in a study of calcite aggregate compaction in the presence of aqueous fluids under similar stresses to those here [67], the subcritical crack mechanism was discounted based on acoustic emission and grain size-strain rate data.

#### 4. Pressure solution creep

The continuous strain evolution during the course of each experiment, subsequent to the initial fluid injection-compaction step, points to a fluid-assisted deformation mechanism based on chemical reactions between the fluids and the rock cores. At the experimental conditions of low temperature and moderate stresses in the present study, PSC is presumably the principal strain mechanism. Evidence in support of this mechanism is discussed below in the context of conceptual PSC models.

Three primary models have been proposed in the literature to describe the mechanism of PSC: the "thin fluid film" model [30, 31, 53, 54, 63], see Figure 11a; the "island-channel" model [39, 40, 49, 50, 56, 57], see Figure 11b; and the "free face-plastic deformation" model [22, 56, 59, 60], see Figure 11c. These three models, while each being different, share many points in common and thus are not mutually exclusive.

The thin fluid film model postulates that dissolution takes place over the entire grain-grain contact surface within a continuous, strongly adsorbed thin fluid phase trapped in the contact zone. The adsorbed fluid film supports the deviatoric stress normal to the grain-grain interface. Removal of dissolved material occurs via diffusion within the thin fluid film, at rates that are theoretically estimated to be 10 to 100 times lower compared to free (pore) fluids [1, 18]. In the island-channel model, individual grain-grain contacts are characterized by numerous island structures that support the normal stress between grains, separated by channels containing fluid at pore pressure (i.e. channels connected to pore spaces).

Some studies consider the presence of a trapped thin fluid film within the island structures (i.e., 'wet' island-channel); in this case, dissolution and diffusion within the trapped fluid remove dissolved material and lead to compaction [39, 49, 56]. Others consider dry island contacts that are subject to undercutting by dissolution in the channels, followed by island collapse via cataclasis and, or plastic flow [56]. And finally, the free face-plastic deformation model considers a continuous grain-grain contact without a fluid film. Dissolution of the grain-grain contact in the pore fluid causes undercutting of the contact zone, and once a critical diameter is reached the grain-grain contact collapses either by plastic flow or brittle failure. This model is practically identical to the 'dry' island-channel model, except for the scale. Each of these three mechanistic models can be described by constitutive laws that include both macroscopic and microscopic parameters [20, 39].

It is possible that all 3 processes occurred simultaneously during the deformation of the four cores. However, estimating the spatial and temporal partitioning of the PSC mechanisms remains a challenge, and thus could only be approached in a qualitative manner. We first examine what can be termed uniform and 'rapid' compaction. This occurred at the beginning of each experiment (after initial compaction due to injection of fluids), and was in general associated with fluid flow, especially in the presence of high $P_{CO_2}$ fluids. Rapid compaction was most likely caused by elevated dissolution kinetics due to the action of low pH, chemically unsaturated fluids in the pore spaces, and probably involved undercutting of grain-grain or island contacts, via the free face and, or the 'dry' island-channel mechanism; in both cases this would have involved cataclastic and, or plastic compaction. Given that the fluid chemistry became less aggressive as the fluid traversed the cores (i.e., pore fluids became more saturated, pH increased), it can be assumed that rapid compaction of the cores was favored in the inlet regions, as evidenced by the CT images in Figure 9. The second type of rapid compaction behavior, associated with transient high strain events (as exemplified by the Estaillades limestone and the sandstone in the presence of high $P_{CO_2}$ fluids), was not temporally restricted to the beginning of each experiment. Transient compaction, however, always occurred in the presence of high $P_{CO_2}$ fluids, indicating a strong link to the dissolving action of low pH, aggressive pore fluids. What sets these transient events apart are their short durations and very high strain rates, leading us to speculate that these processes commenced with the simultaneous collapse of multiple weakened grain-grain or island-channel structures (created by dissolution undercutting). Moreover, the initial collapse of just a few contacts may have led to a cascading effect, which set off a larger-scale collapse process, resulting, for example, in the largest strain event measured in this study (see Figure 4, event 'g'). These sudden compaction events may also have been spatially localized within inlet regions of the cores. It is possible to speculate even further, in

particular with respect to a single experiment, e.g. Estaillades (Figure 4), by proposing that the 'staircase' pattern of compaction (i.e. slow-fast-slow...) illustrated in Figure 12 indicates a series of recurrent events associated with several PSC mechanisms: slow and continuous compaction via a combination of dissolution, undercutting, and thin film diffusion leading to weakened grain-grain or island-channel structures (the slow step); the weakened structures then periodically collapse by cataclasis (the fast step); a period of slow compaction starts again. The possible continuity of this type of compaction behavior, in the presence of continuously injected high $P_{CO_2}$ fluids, cannot be ascertained.

Long-term compaction behavior characterized by extended periods of uniform and relatively slow strain rates was generally measured in the absence of fluid flow, indicating a possible link with pore fluids that were close to chemical saturation (or even oversaturated, see Table IV and Figure 10c). We argue that such conditions should have diminished the role of PSC mechanisms based on rapid dissolution and intergranular collapse, and favored mechanisms based on intergranular dissolution and diffusion. There are two main reasons for this: a) chemical dissolution reactions associated with thin fluid film diffusion in trapped fluid films are likely to produce steady and relatively slow compaction rates; b) the driving force for the intergranular dissolution/diffusion models is based chemical potential differences between intergranular zones and pore spaces (see details in [28], and references therein), and thus, even if the pore fluids were saturated, dissolution and diffusion of material would still occur, ensuring continual deformation. PSC mechanisms based on intergranular dissolution and diffusion most likely were localized in the central and outlet portions of the cores. In general, long-term deformation in the absence of fluid flow will eventually result in nearly all channel and pore fluid volumes evolving to chemical equilibrium with their respective grain surfaces (estimated to be a few days for calcite grains in limestone; and much longer time periods for quartz grains in a sandstone, depending on temperature and other kinetic parameters). Therefore, under (nominal) no-flow conditions and over long time intervals (which may involve time scales exceeding experimental studies), PSC mechanisms based on trapped fluid film dissolution and diffusion should predominate over dissolution-undercutting mechanisms, such as the free face and 'dry' island-channel mechanisms [60].

## V. CONCLUSIONS

Injection of important quantities of $CO_2$ into aquifers and other underground geological sequestration sites will have important consequences in terms of the physical and chemical evolution of the water-rock system, and in particular, affecting the fluid transport properties and mechanical stability of the reservoir. Important parame-

ters determining the long-term behavior of sequestration sites are the lithology-mineralogy of the host rock, fluid chemistry, injection rate, $T$, $P$ and stress conditions of the reservoir. One of the major findings of this experimental study is that fluids with a high $P_{CO_2}$ have the potential for aggressively dissolving rocks (in particular carbonate lithologies whose reactivity is very sensitive to pH and $P_{CO_2}$) and creating zones of elevated porosity. Both of these phenomena lead to enhanced strain and strain rates. This effect will be particularly pronounced in the immediate vicinity of the $CO_2$-injection wells. Injection of $CO_2$ may, in fact, be viewed as a well stimulation technique, in that low pH fluids will dissolve and enlarge pre-existing fracture systems plugged with secondary minerals, thereby enhancing the fracture network and aiding permeability development. The results from this experimental study, combined with complementary theoretical studies (e.g. [52]), point out that percolation of $CO_2$-rich fluids can influence the compaction behavior of an aquifer, and thereby affect its long-term $CO_2$ storage and sequestration capacity. The effect of compaction and reduced $CO_2$ storage capacity can be potentially off-set by relying on high flow rate injections that can aid in the far-field dispersion of acidic, high $P_{CO_2}$ fluid plumes.

[1] Alcantar, N., J. Israelachvili, and J. Boles (2003), Forces and ionic transport between mica surfaces: Implication for pressure solution, *Geochim. Cosmochim. Acta*, *67*(7), 1289–1304.

[2] Arts, R., P. Zweigel, and A. Lothe (2000), Reservoir geology of the Utsira sand in the southern Viking Graben area - a site for potential $CO_2$ storage, *EAGE $62^{nd}$ Conference and Technical Edition, Glasgow, Scotland*, pp. Paper B–20.

[3] Atkinson, B. K. (1984), Subcritical crack growth in geological materials, *J. Geophys. Res.*, *89*(B6), 4077–4114.

[4] Baklid, A., R. Korbul, and G. Owren (1996), Sleipner Vest $CO_2$ disposal, $CO_2$ injection into a shallow underground aquifer, *Presented on the 1996 SPE Annual technical Conference and Exhibition, Denver, Colorado, USA, SPE paper 36600*, pp. 1–9.

[5] Brady, P. V., and J. V. Walther (1990), Kinetics of quartz dissolution at low temperatures, *Chem. Geol.*, *82*, 253–264.

[6] Busenberg, E., and L. N. Plummer (1986), A comparative study of the dissolution and crystal growth kinetics of calcite and aragonite., in *Studies in Diagenesis*, vol. 105, edited by F. Mumpton, pp. 139–168, U.S.G.S. Bulletin 1578, U.S. Geological Survey.

[7] Carroll, S. A., and K. G. Knauss (2005), Dependence of labradorite dissolution kinetics on $CO_2$(aq), Al(aq), and temperature, *Chem. Geol.*, *217*, 213–225.

[8] Chadwick, R. A., P. Zweigel, U. Gregersen, G. A. Kirby, S. Holloway, and P. N. Johannessen (2002), *Geological Characteristics of $CO_2$ Storage Sites: Lessons from Sleipner, Northern North Sea*, pp. B1–3, Elsevier.

[9] Chester, F. M., J. S. Chester, A. K. Kronenberg, and A. Hajash (2007), Subcritical creep compaction of quartz sand at diagenetic conditions: Effects of water and grain size, *Submitted to JGR*.

[10] Cox, S. F., and M. S. Patterson (1991), Experimental dissolution-precipitation creep in quartz aggregates at high temperatures, *Geophys. Res. Lett.*, *18*, 1401–1404.

[11] De Marsily, G. (1986), *Quantitative hydrogeology*, Academic Press, New York.

[12] de Meer, S., and C. J. Spiers (1995), Creep of wet gypsum aggregates under hydrostatic loading conditions, *Tectonophysics*, *245*, 171–183.

[13] de Meer, S., and C. J. Spiers (1997), Uniaxial compaction creep of wet gypsum aggregates, *J. Geophys. Res.*, *102*(B1), 875–891.

[14] de Meer, S., and C. J. Spiers (1999a), Influence of pore-fluid salinity on pressure solution creep gypsum, *Tectonophysics*, *308*(3), 311–330.

[15] de Meer, S., and C. J. Spiers (1999b), On Mechanisms and Kinetics of Creep by Intergranular Pressure solution, in *Growth, Dissolution and Pattern Formation in Geosystems*, edited by B. Jamtveit and P. Meakin, pp. 345–366, Kluwer Academic Publishers.

[16] den Brok, S. W. J. B., J. Morel, and M. Zahid (2002), In situ experimental study of roughness development at a stressed solid/fluid interface, in *Deformation Mechanisms, Rheology and Tectonics : Current Status and Future Perspectives*, vol. 200, edited by S. de meer, M. Drury, J. de Bresser, and G. Pennock, pp. 73–83, Geological Society Special Publications, London.

[17] Dewers, T., and A. Hajash (1995), Rate laws for water assisted compaction and stress-induced water-rock interaction in sandstones, *J. Geophys. Res.*, *100*(B7), 13,093–13,112.

[18] Dysthe, D. K., F. Renard, F. Porcheron, and B. Rousseau (2002), Fluid in mineral interfaces–molecular simulations of structure and diffusion, *Geophy. Res. Lett.*, *29*(7).

[19] Emberley, S., I. Hutcheon, M. Shevalier, K. Durocher, B. Mayer, W. D. Gunter, and E. H. Perkins (2005), Mon-

itoring of fluid–rock interaction and $CO_2$ storage through produced fluid sampling at the Weyburn $CO_2$–injection enhanced oil recovery site, Saskatchewan, Canada, *Appl. Geochem.*, *20*(6), 1131–1157.

[20] Evans, B., and D. L. Kohlstedt (1995), Rheology of rocks, in *Rock Physics and Phase Relations: A Handbook of Physical Constants*, edited by T. Ahrens, American Geophysical Union, Washington.

[21] Gale, J., N. P. Christensen, A. Culter, and T. A. Torp (2001), Demonstrating the Potential for Geological Storage of $CO_2$: the Sleipner and GESTCO Projects, *Env. Geosciences*, *8*(3), 160–165.

[22] Green, H. (1984), Pressure solution creep: Some causes and mechanism, *J. Geophys. Res.*, *89*, 4313–4318.

[23] Guichet, X., J. Schott, E. H. Oelkers, B. Vincent, C. Magnier, and E. Brosse (2005), Reactive transport experiments and modelling of $CO_2$ sequestration in deep aquifers, *Geoch. Cosmoch. Acta (Abstracts of the 15th Goldschmidt Conference, Moscow Idaho, USA, 2005)*, *69*(N.10 S), A 179.

[24] Hajash, A. J., and M. Bloom (1991), Marine diagenesis of feldspathic sand: A flow-through experimental study at $200°C$, 1 kbar, *Chem. Geol.*, *89*, 359–377.

[25] He, W., A. Hajash, and D. Sparks (2003), Creep compaction of quartz aggregates: effects of pore-fluid flow - A combined experimental and theoretical study, *Am. J. Sci.*, *303*, 73–93.

[26] Hellmann, R., and D. Tisserand (2006), Dissolution kinetics as a function of the Gibbs free energy of reaction: An experimental study based on albite feldspar, *Geochim. Cosmochim. Acta*, *70*, 364–383.

[27] Hellmann, R., J.-P. Gratier, and T. Chen (1998), Mineral-water interactions and stress: pressure solution of halite aggregates, in *Water-Rock Interaction WRI-9*, edited by G. B. Arehart and J. Hulston, pp. 777–780, A. A. Balkema, Rotterdam.

[28] Hellmann, R., P. J. N. Renders, J.-P. Gratier, and R. Guiguet (2002a), Experimental pressure solution compaction of chalk in aqueous solutions. Part 1. Deformation behavior and chemistry, in *Water-rock Interaction, Ore Deposits, and Environmental Geochemisty: A tribute to David A. Crerar*, vol. 7, edited by R. Hellmann and S. A. Wood, pp. 129–152, The Geochemical Society, Special Publication.

[29] Hellmann, R., P. Gaviglio, P. J. N. Renders, J.-P. Gratier, S. Békri, and P. Adler (2002b), Experimental pressure solution compaction of chalk in aqueous solutions. Part 2. Deformation examined by SEM, porosimetry, synthetic permeability, and X-ray computerized tomography, in *Water-rock Interaction, Ore Deposits, and Environmental Geochemisty: A tribute to David A. Crerar*, vol. 7, edited by R. Hellmann and S. A. Wood, pp. 153–178, The Geochemical Society, Special Publication.

[30] Hickman, S. H., and B. Evans (1991), Experimental pressure solution in halite : the effect of grain/interphase boundary structure, *J. Geol. Soc.*, *148*(3), 549–560.

[31] Hickman, S. H., and B. Evans (1995), Kinetics of pressure solution at halite-silica interfaces and intergranular clay films, *J. Geophys. Res.*, *100*(B7), 13,113–13,132.

[32] Honeyborne, D. B. (1982), The building limestones of France, *Tech. rep.*, Building Research Establishment Report.

[33] Ioannou, I., W. D. Hoff, and C. Hall (2004), On the role of organic adlayers in the anomalous water sorptivity of the Lépine limestone, *J. Colloid Interface Sci.*, *279*, 228–234.

[34] Johnson, J. W., and J. J. Nitao (2002), *Proc. of the $6^{th}$ International Conf. on Greenhouse Gas Control Technologies, Kyoto, Japan*, chap. Reactive transport modeling of geologic $CO_2$ sequestration at Sleipner, Pergamon.

[35] Johnson, J. W., E. H. Oelkers, and H. C. Helgeson (1992), SUPCRT92: A software package for calculating the standard modal thermodynamic properties of minerals, gases, aqueous species, and reactions from 1 to 5000 bars and $0°C$ to $1000°C$, *Computers and Geosciences*, *18*, 899–947.

[36] Knauss, K. G., and T. J. Wolery (1988), The dissolution kinetics of quartz as a function of pH and time at $70°C$, *Geochim. Cosmochim. Acta*, *52*, 43–53.

[37] Krumhansl, J. L., H. R. Westrich, and C. Jove-Colon (2003), Geochemical implications of $CO_2$ sequestration in arkosic sandstone reservoirs, in *$2^{nd}$ Annual Conference on Carbon Sequestration*.

[38] Lackner, K. S. (2003), A guide to $CO_2$ sequestration, *Science*, *300*, 1677–1678.

[39] Lehner, F. K. (1995), A model for intergranular pressure solution in open systems, *Tectonophysics*, *245*(3-4), 153–170.

[40] Lehner, F. K., and J. Bataille (1984), Non-equilibrium thermodynamics of pressure solution, *Pure and Applied Geophysics*, *122*, 53–85.

[41] Lockner, D. (1993), Room temperature creep in saturated granite, *J. Geophys. Res.*, *98*, 475–487.

[42] Luo, H. A., and G. J. Weng (1987), On Eshelby's inclusion problem in a three-phase spherically concentric solid, and a modification of Mori-Tanaka's method, *Mech. Materials*, *6*(4), 347–361.

[43] Moberg, R. (2001), The Weyburn $CO_2$ Monitoring and Storage Project, *Greenhouse Issues, IEA Greenhouse Gas R&D*, *57*.

[44] Niemeijer, A., C. J. Spiers, and B. Bos (2002), Compaction creep of quartz sand at $400$-$600°C$: Experimental evidence for dissolution-controlled pressure solution, *Earth and Planetary Science Letters*, *195*, 261–275.

[45] Plummer, L. N., and E. Busenberg (1982), The solubilities of calcite, aragonite and vaterite in $CO_2$-$H_2O$ solutions between 0 and $90°C$, and evaluation of the aqueous model for the system $CaCO_3$-$CO_2$-$H_2O$, *Geochim. Cosmochim. Acta*, *46*(6), 1011–1040.

[46] Poirier, J.-P. (1995), Plastic rheology of crystals, in *Mineral physics and crystallography. A handbook of physical constants*, edited by T. J. Arhens, American Geophysical Union.

[47] Pokrovsky, O. S., S. V. Golubev, and J. Schott (2005), Dissolution kinetics of calcite, dolomite and magnesite at $25°C$ and 0 to 50 atm $pCO_2$, *Chem. Geol.*, *217*(3-4), 239–255.

[48] Preston, C., M. Monea, W. Jazrawi, K. Brown, S. Whittaker, D. White, D. Law, R. Chalaturnyk, and B. Rostron (2005), IEA GHG Weyburn $CO_2$ monitoring and storage project, *Fuel Processing Technology*, *86*(14-15), 1547–1568.

[49] Raj, R. (1982), Creep in polycrystalline aggregates by matter transport through a liquid phase, *J. Geophys. Res.*, *87*(2), 4731–4739.

[50] Raj, R., and C. K. Chyung (1981), Solution-precipitation creep in glass ceramics, *Acta Metallurgica*, *29*(1), 159–166.

[51] Renard, F., D. Dysthe, J. Feder, K. Bjrlykke, and

B. Jamtveit (2001), Enhanced pressure solution creep rates induced by clay particles: Experimental evidence in salt aggregates, *Geophy. Res. Lett.*, *28*(7), 1295–1298.

[52] Renard, F., E. Gundersen, R. Hellmann, M. Collombet, and Y. Le Guen (2005), Numerical modeling of carbon dioxide sequestration on the rate of pressure solution creep in limestone: Preliminary results, *Oil & Gas Science and Technology - Rev. IFP*, *60*(2), 381–399.

[53] Rutter, E. H. (1976), The kinetics of rock deformation by pressure solution, *Philos. Trans. R. Soc. Lond., A, Mathematical and Physical Sciences*, *283*, 203–219.

[54] Rutter, E. H. (1983), Pressure solution in nature, theory, and experiment, *J. Geol. Soc., London*, *140*(5), 725–740.

[55] Schutjens, P. M. T. M. (1991), Experimental compaction of quartz sand at low effective stress and temperature conditions, *J. Geol. Soc. London*, *148*, 527–539.

[56] Spiers, C. J., and R. H. Brezesowsky (1993), Densification behaviour of wet granular salt: Theory versus experiment, in *Seventh Symposium on Salt vol.I*, edited by H. Kakihana, J. H. R. Hardy, T. Hoshi, and K. Toyokura, pp. 83–92, Elsevier Sciences, Amsterdam.

[57] Spiers, C. J., and P. M. T. M. Schutjens (1990), Densification of crystalline aggregates by fluid-phase diffusional creep, in *Deformation processes in minerals, ceramics and rocks*, vol. 1, edited by D. J. Barber, pp. 334–353, Unwin Hyman, London.

[58] Spycher, N., K. Pruess, and J. Ennis-King (2003), $CO_2$-$H_2O$ mixtures in the geological sequestration of $CO_2$. I. Assessment and calculation of mutual solubilities from 12 to 100°C and up to 600 bar, *Geochim. Cosmochimi. Acta*, *67*(16).

[59] Tada, R., and R. Siever (1986), Experimental knife-edge pressure solution of halite, *Geochim. Cosmochimi. Acta*, *50*(1), 29–36.

[60] Tada, R., R. Maliva, and R. Siever (1987), A new mechanism for pressure solution in porous quartzose sandstone, *Geochim. Cosmochimi. Acta*, *51*(9).

[61] van der Lee, J. (1993), Chess, another speciation and surface complexation computer code, *Tech. Rep. LHM/RD/93/99*, CIG-Ecole des Mines de Paris, Fontainebleau, France.

[62] Wawersik, W. G., et al. (2001), Terrestrial sequestration of $CO_2$: An assessment of research needs, in *Advances in Geophysics*, vol. 43, edited by R. Dmowska, pp. 97–177, Havard University, Cambridge, MA, USA.

[63] Weyl, P. K. (1959), Pressure solution and the force of crystallization - a phenomenological problem, *J. Geophys. Res.*, *64*(11), 2001–2025.

[64] Whittaker, S. G., and B. Rostron (2002), *Geological Storage of $CO_2$ in a Carbonate Reservoir within the Williston Basin, Canada: An Update*, chap. D1-1, Elsevier.

[65] Wolery, T. J. (1992), EQ3NR, A Computer Program for Geochemical Aqueous Speciation–Solubility Calculations: Theoretical Manual, User's Guide, and Related Documentation (Version 7.0), *Tech. Rep. UCRL-MA-110662 PT III.*, Lawrence Livermore Natl. Lab.

[66] Zhang, X., and C. J. Spiers (2005a), Compaction of granular calcite by pressure solution at room temperature and effects of the pore fluid chemistry, *Int. J. Rock Mech. Mining Sci.*, *42*(7-8), 950–960.

[67] Zhang, X., and C. J. Spiers (2005b), Effects of phosphate ions on intergranular pressure solution in calcite: an experimental study, *Geochim. Cosmochim. Acta*, *69*(24), 5681–5691.

[68] Zoubstov, S., F. Renard, J.-P. Gratier, R. Guiguet, D. K. Dysthe, and V. Traskine (2004), Experimental pressure solution creep of polymineralic aggregates, *Tectonophysics*, *385*, 45–57.
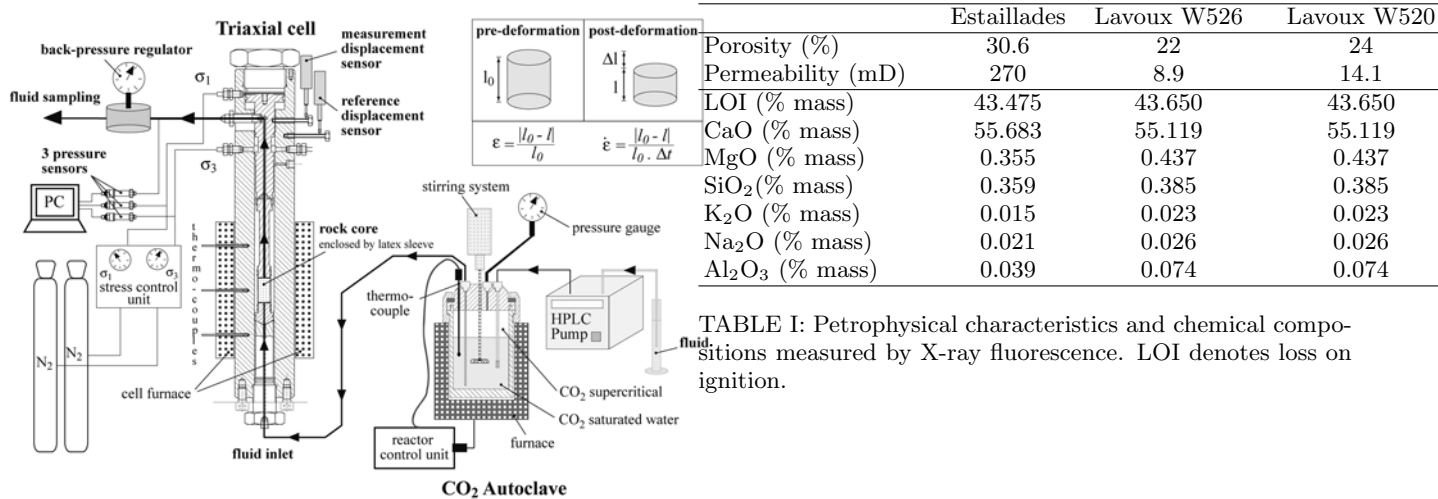
FIG. 1: Triaxial cell used for measuring axial strain in presence $H_2O$-$CO_2$ fluids. Vertical stress $\sigma_1$, lateral stress $\sigma_3$ ($=\sigma_2$), temperature, fluid pressure $P_f$, and injection rate were all separately controlled and measured. High $P_{CO_2}$ fluids were prepared in separate autoclave. Inset shows expressions for strain, $\epsilon$ and strain rate, $\dot{\epsilon}$.

|  | Estaillades | Lavoux W526 | Lavoux W520 |
|---|---|---|---|
| Porosity (%) | 30.6 | 22 | 24 |
| Permeability (mD) | 270 | 8.9 | 14.1 |
| LOI (% mass) | 43.475 | 43.650 | 43.650 |
| CaO (% mass) | 55.683 | 55.119 | 55.119 |
| MgO (% mass) | 0.355 | 0.437 | 0.437 |
| $SiO_2$(% mass) | 0.359 | 0.385 | 0.385 |
| $K_2O$ (% mass) | 0.015 | 0.023 | 0.023 |
| $Na_2O$ (% mass) | 0.021 | 0.026 | 0.026 |
| $Al_2O_3$ (% mass) | 0.039 | 0.074 | 0.074 |

TABLE I: Petrophysical characteristics and chemical compositions measured by X-ray fluorescence. LOI denotes loss on ignition.
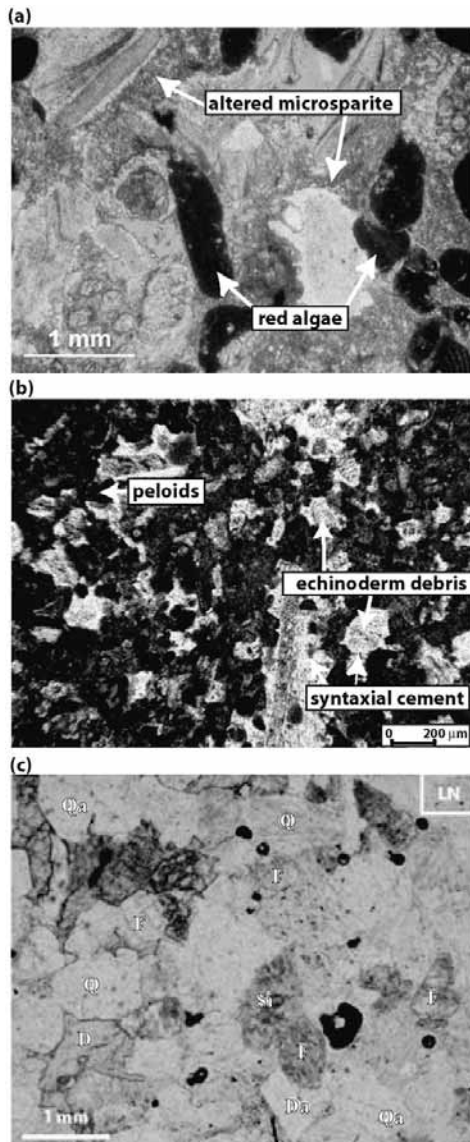
FIG. 2: Thin sections of rock samples (a) Estaillades limestone sample is composed of red algae debris (dark grains) and calcic shells embedded into a microsparitic cement (blue is epoxy resin); (b) Lavoux limestone contains echinoderm clasts and calcic peloids embedded into a calcite cement (red is epoxy resin); (c) arkosic sandstone composed of quartz and feldspar grains cemented by dolomite and lesser amounts of calcite. (D: dolomite, Da: idiomorphic dolomite, F: feldspar, Q: quartz, Qa: idiomorphic quartz, Si: chalcedony).

FIG. 3: Initial compaction induced by injection of fluids into dry, stressed samples. The initial Lavoux strains were not dependent on $P_{CO_2}$, suggesting a pore pressure– mechanical effect. Total strain is also a function of $\sigma_e$.
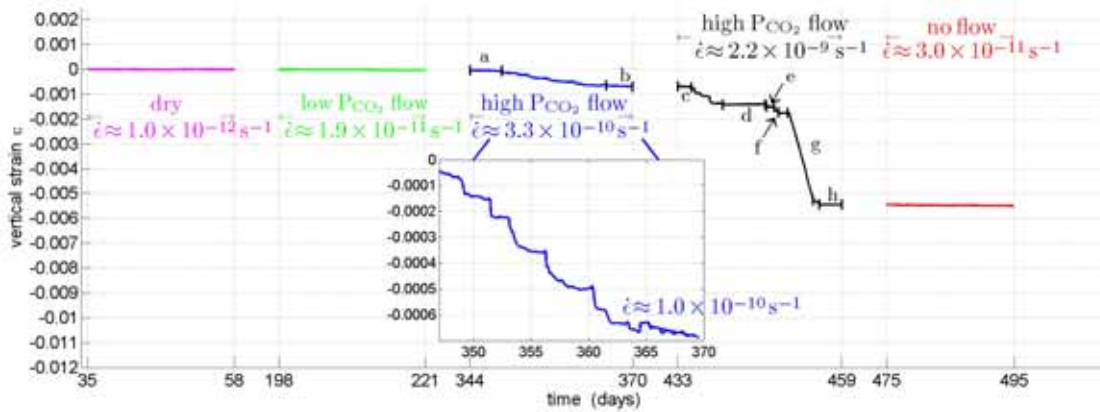♣ : fluid pressure variation



FIG. 4: Vertical axial deformation of Estaillades limestone sample. Separate $\epsilon$-time segments representative of five experimental periods during which average strain rates were determined (indicated directly in the diagram above). Time periods where no data are shown represent non stable-conditions due to experimental parameter changes (fluid $P_{CO_2}$, temperature, $\sigma_e$). The magenta curve represents dry deformation under stress. Injection of water at low $P_{CO_2}$ (green curve) followed, causing compaction and increasing the strain rate by one order of magnitude. A simultaneous change in temperature (25 to 80 °C) and injection of high $P_{CO_2}$ water (blue curve) caused a significant increase in strain and strain rate, characterized by a staircase pattern of alternating moderate strain rates and sudden transient strain rate increases. The strain rate behavior was amplified further on in time (black curve), especially noteworthy at 450-454 days. The strain rate decreased and became steady again (red curve) when the injection of high $P_{CO_2}$ water was stopped. A few individual strain rate estimates for the high $P_{CO_2}$ regime (blue and black curves) are listed here (strain rate intervals on diagram): a. $\dot{\epsilon} = 1.5 \times 10^{-10}$ s$^{-1}$ b. $\dot{\epsilon} = 1.0 \times 10^{-10}$ s$^{-1}$ c. $\dot{\epsilon} = 1.4 \times 10^{-10}$ s$^{-1}$ d. $\dot{\epsilon} = -4 \times 10^{-11}$ s$^{-1}$ e. $\dot{\epsilon} = 6.0 \times 10^{-11}$ s$^{-1}$ f. $\dot{\epsilon} = -6.3 \times 10^{-9}$ s$^{-1}$ g. $\dot{\epsilon} = 1.1 \times 10^{-8}$ s$^{-1}$ h. $\dot{\epsilon} = 0.0$ s$^{-1}$, note that $\dot{\epsilon} < 0$ indicates vertical dilation.
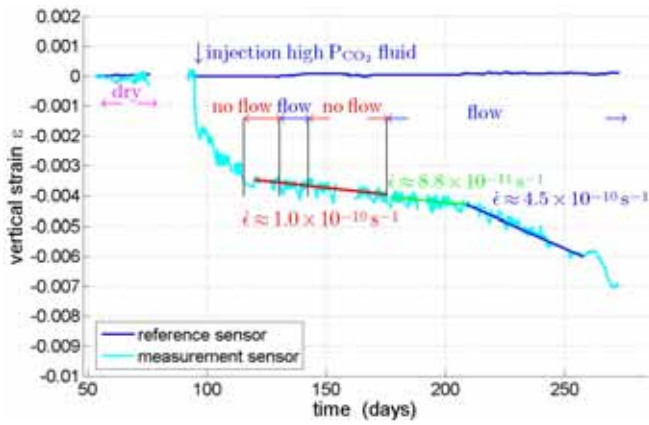
FIG. 5: Vertical axial strain deformation measured for Lavoux W526 sample in the absence of fluid and during injection of high $P_{CO_2}$ saline fluid (cyan curve). Time periods with no data represent non–stable conditions associated with parameter changes. The red time period $\dot{\epsilon}$ includes a short flow period. Note that the renewed injection of high $P_{CO_2}$ saline solution caused a large increase in $\dot{\epsilon}$, but after time lag of $\approx$ 40 days. The end of the experiment was marked by a sudden, rapid increase in strain and strain rate.
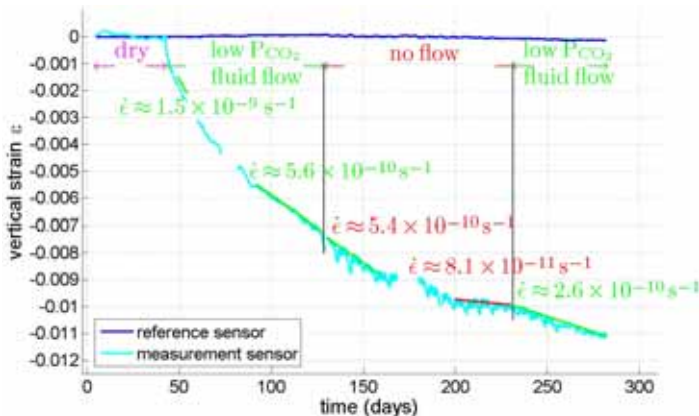


FIG. 6: Vertical axial strain measured for Lavoux W520 limestone (green line) compared to reference displacement sensor (blue line). At dry conditions under stress no measurable compaction occurred. Time periods with no data represent non stable conditions associated with parameter changes. Injection of low $P_{CO_2}$ saline fluid caused immediate compaction; the strain rate gradually decreased with time. Stopping the injection had no effect on $\dot{\epsilon}$ until $\approx$ day 170. Loss of data starting at $t =$ 168 day is represented by a false strain plateau. Renewal of fluid injection caused an immediate increase in $\dot{\epsilon}$ at end of experiment.
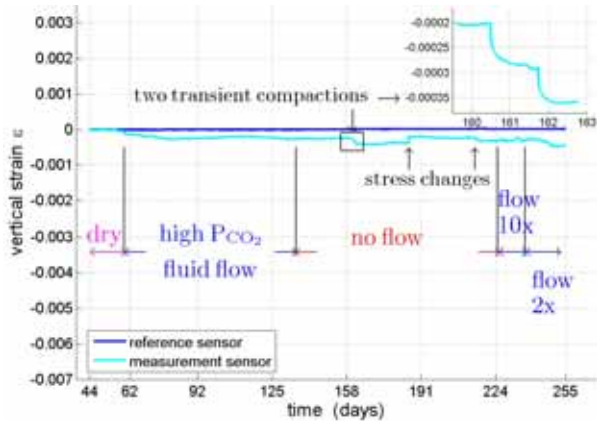
FIG. 7: Vertical strain measured on arkosic sandstone. No measurable strain was detected at dry conditions. Injection of high $P_{CO_2}$ saline solution caused measurable strain to occur. Two sudden transient strain events occurred at days 160.5 and 161.8. A short period of vertical stress decrease and increase resulted in immediate responses in the strain curve. When flow was re-initiated, injection rate was 10x and the 2x the initial rate.

| Rock sample | Estaillades | | Lavoux W526 | Lavoux W520 | Sandstone |
|---|---|---|---|---|---|
| Fluid $P_{CO_2}$ | low $P_{CO_2}$ | high $P_{CO_2}$ | high $P_{CO_2}$ | low $P_{CO_2}$ | high $P_{CO_2}$ |
| $\sigma_1$ (MPa) | 8.9 | 10.0 | 16.3 | 16.3 | 16.0 |
| $\sigma_3$ (MPa) | 7.3 | 8.5 | 12.0 | 11.6 | 10.2 |
| $p_f$ (MPa) | 5.9 | 7.8 | 7.9 | 7.9 | 8.3 |
| $\sigma_e$ (MPa) | 3.0 | 2.2 | 8.4 | 8.4 | 7.7 |
| $P_{CO_2}$ (MPa) | $10^{-4.5}$ | 7.8 | 7.9 | $10^{-4.5}$ | 8.3 |
| T (°C) | 25 | 80 | 40 | 40 | 40 |
| [NaCl] (mol.l$^{-1}$) | 0 | 0 | $10^{-2}$ | $10^{-2}$ | $10^{-2}$ |
| Fluid flow (m$^3$.s$^{-1}$) | $8.33 \times 10^{-11}$ | $8.33 \times 10^{-11}$ | $8.33 \times 10^{-11}$ | $8.33 \times 10^{-11}$ | $8.33 \times 10^{-11}$ |
| Residence time (h) | 20.5 | 20.5 | 12.8 | 14.0 | 10.0 |
| Fluid velocity (m.s$^{-1}$) | $6 \times 10^{-7}$ | $6 \times 10^{-7}$ | $1 \times 10^{-6}$ | $9 \times 10^{-7}$ | $1.4 \times 10^{-6}$ |

TABLE II: Experimental parameters during compaction.

| | Dry (s$^{-1}$) | Low $P_{CO_2}$ fluid flow (s$^{-1}$) | Low $P_{CO_2}$ no flow (s$^{-1}$) | High $P_{CO_2}$ fluid flow (s$^{-1}$) | High $P_{CO_2}$ no flow (s$^{-1}$) |
|---|---|---|---|---|---|
| Estaillades | $1.0 \times 10^{-12}$ day 35−58 | $1.9 \times 10^{-11}$ day 198−221 | – – | $1.0 \times 10^{-10}$ day 366−370 | $3.0 \times 10^{-11}$ day 475−495 |
| Lavoux - W526 | $\approx 0$ day 53−74 | – | – | $4.5 \times 10^{-10}$ day 209−258 | $1.0 \times 10^{-10}$ day 120−175 |
| Lavoux - W520 | $1.1 \times 10^{-11}$ day 26−41 | $2.6 \times 10^{-10}$ day 231−282 | $8.1 \times 10^{-11}$ day 200−230 | – | – |
| Sandstone | – | – | – | $2.3 \times 10^{-11}$ day 59−134 | $4.6 \times 10^{-12}$ day 153−161 |

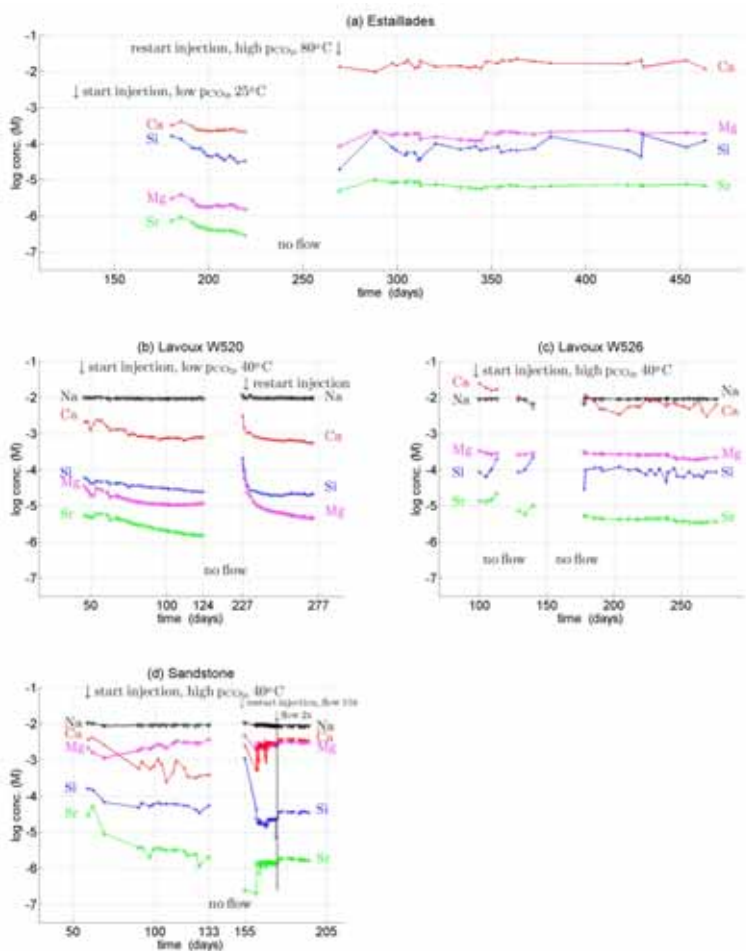TABLE III: Average strain rates with indicated time ranges.

FIG. 8: Time evolution of aqueous concentrations of selected elements collected at outlet of triaxial cell. Fluid $P_{CO_2}$, temperature, and period of no–flow indicated directly on diagrams. After re-initiation of injection, elemental concentrations of the first sample taken were used to estimate concentrations of pore fluids during the preceding no-flow condition.

| [kJ.mol$^{-1}$] | $\Delta G$ Calc. | $\Delta G$ Dolo. | $\Delta G$ Quartz | $\Delta G$ Chalc. | $\Delta G$ Crist. | $\Delta G$ Arag. |
|---|---|---|---|---|---|---|
| Estaill. - low $P_{CO_2}$ - flow | +1.52 | -2.20 | -2.36 | -3.91 | -5.51 | +0.69 |
| Estaill. - low $P_{CO_2}$ - no flow | +2.94 | +0.52 | -2.46 | -4.01 | -5.60 | +2.12 |
| Estaill. - high $P_{CO_2}$ - flow | -0.56 | -4.69 | -5.79 | -7.33 | -8.82 | -1.52 |
| Estaill. - high $P_{CO_2}$ - no flow | +2.12 | -0.46 | -0.30 | -1.14 | -3.33 | +1.15 |
| W520 - low $P_{CO_2}$ - no flow | +13.81 | +28.04 | -8.83 | -10.38 | -11.94 | +12.94 |
| W520 - low $P_{CO_2}$ - flow | +6.68 | +8.78 | -7.36 | -8.91 | -10.47 | +5.81 |
| W526 - high $P_{CO_2}$ - flow | -11.59 | -23.97 | -2.00 | -3.55 | -5.12 | -12.45 |
| W526 - high $P_{CO_2}$ - no flow | -7.07 | -16.18 | -1.69 | -3.24 | -4.80 | -7.93 |
| sandstone - high $P_{CO_2}$ - flow ini. | -20.45 | -28.03 | -3.29 | -4.84 | -6.40 | -21.32 |
| sandstone - high $P_{CO_2}$ - no flow | -13.87 | -16.89 | +4.46 | +3.09 | +1.52 | -14.03 |
| sandstone - high $P_{CO_2}$ - flow 10x | -13.99 | -20.70 | -5.50 | -7.05 | -8.61 | -14.86 |
| sandstone - high $P_{CO_2}$ - flow 2x | -12.67 | -18.10 | -4.26 | -5.81 | -7.37 | -13.52 |

TABLE IV: Chemical saturation state, based on the outlet chemistry, expressed in term of Gibbs free energy of reaction ($\Delta G$) for some common mineral phases relevant to limestone and sandstone deformation. Negative $\Delta G$ values indicate undersaturation, positive values indicate supersaturation. Calc.: calcite; Dolo.: dolomite; Chal.: chalcedony; Crist.:cristobalite; Arag.: aragonite
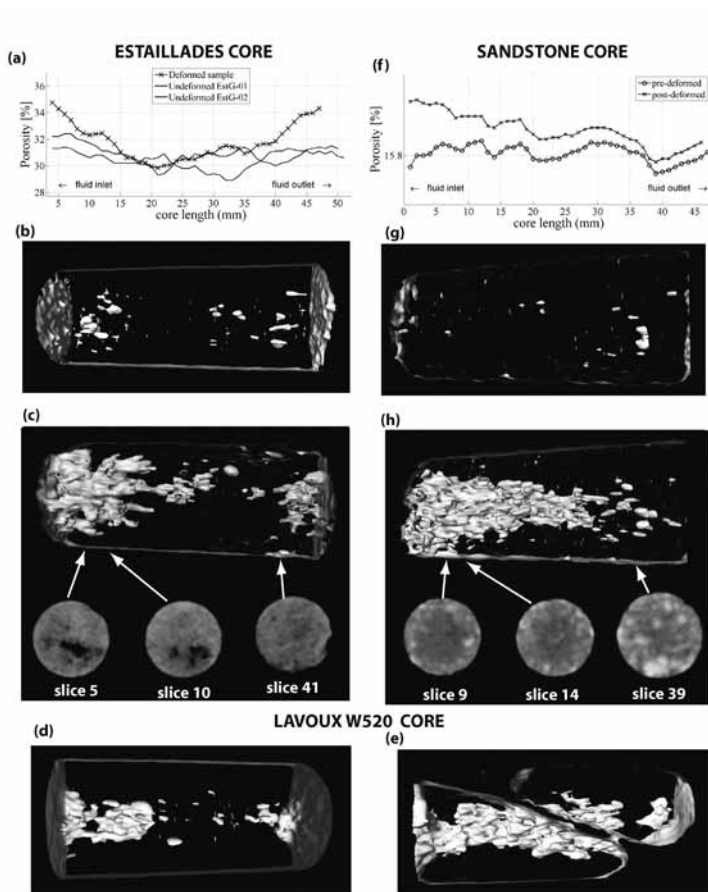
FIG. 9: X-ray computed tomography (CT) profiles and images of samples before and after deformation. All core lengths equaled 45-50 mm. (a) CT-based porosity profile of deformed Estaillades limestone, compared to 2 different undeformed samples. Note elevated porosities in inlet and outlet regions after deformation. (b) CT image (1600 attenuation) of an Estaillades limestone before deformation (corresponds to porosity profile EstG-02 in (a)). (c) CT image (1600 attenuation) of deformed Estaillades limestone (different sample than in (b)). Note CT density slices and locations in core, porous channel-like regions appear black in slices 5 and 10. (d) CT image (1965 attenuation) of Lavoux W520 before deformation. (e) CT image (1965 attenuation) of same Lavoux W520 after deformation. Note development of axial porosity. Non-continuity of sample due to post-experiment shear damage. (f) CT-based porosity profile of sandstone before and after deformation. Pre-deformation porosity based on independent measurement, post-deformation porosity cannot be quantified due to lack of CT calibration. (g) CT image (1290 attenuation) of sandstone before deformation. (h) CT image (1290 attenuation) of same sandstone after deformation, showing extensive axial porosity development. Note CT density slices and locations in core.
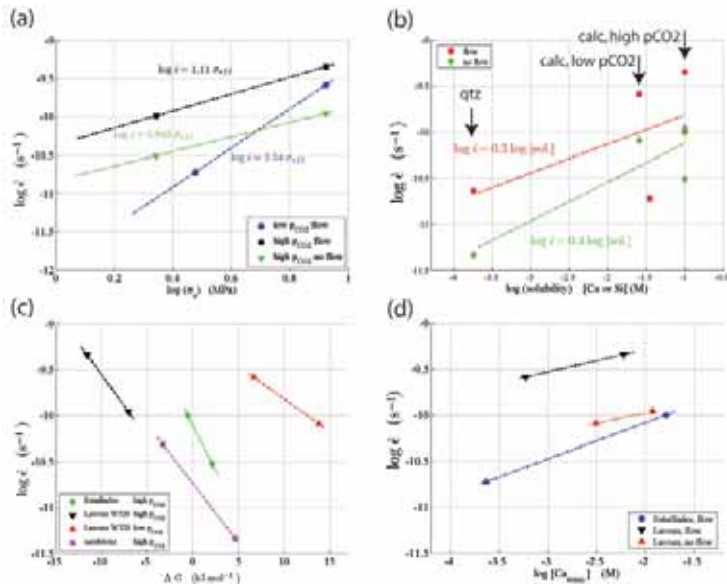
FIG. 10: (a) $\dot{\epsilon}$ as a function of $\sigma_e$. The 3 separate data sets represent limestone deformation in the presence of water at low $P_{CO_2}$-flow; high $P_{CO_2}$-flow; and high $P_{CO_2}$-no flow conditions. Slopes range from 0.9 to 2.5, such values are typical for PSC deformation. (b) $\dot{\epsilon}$ as a function of calcite and quartz solubility (expressed in terms of [Ca] and [Si]), as a function of fluid $P_{CO_2}$. The vertically–paired data sets represent fluid flow and no-flow deformation conditions. Data pairs with the lowest solubility represent the sandstone, the intermediate solubility data represent the limestone at low $P_{CO_2}$, and the highest solubility data represent limestones at high $P_{CO_2}$. Note also that flow strain rates were always higher than their no-flow counterparts. The measured slopes equal 0.3 and 0.4 for the flow and no-flow regimes, respectively. (c) $\dot{\epsilon}$ as a function of solution saturation expressed in terms of $\Delta G$ for calcite and quartz dissolution. The 4 data groups represent the 3 limestone samples and the sandstone, and each data pair represents flow and no-flow conditions. Negative values of $\Delta G$ denote fluid undersaturation, positive values supersaturation. Negative slopes indicate that with increasing pore fluid saturation, the strain rate decreases. (d) $\dot{\epsilon}$ as a function of output [Ca] for the 3 limestones. The 3 data groups represent Estaillades at low $P_{CO_2}$, high $P_{CO_2}$, flow; Lavoux low $P_{CO_2}$, high $P_{CO_2}$, flow; Lavoux low $P_{CO_2}$, high $P_{CO_2}$, no flow. For any data pair, the positive slopes indicate that the rate of compaction was always greater at conditions of high $P_{CO_2}$.
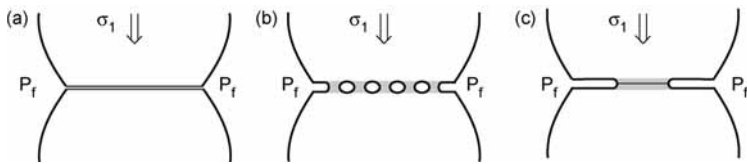
FIG. 11: Schematic illustrations of the 3 different PSC mechanisms. (a) "thin fluid film" model: thin adsorbed intergranular fluid film supports normal stress, with dissolution and diffusion occurring within the film. (b) "island-channel" model: multiple island structures separated by channels containing fluid at pore pressure; stressed islands dissolve preferentially until plastic or brittle failure occurs; alternatively, island structures may contain a trapped fluid film. (c) "free face and plastic deformation" model: dissolution occurs exclusively at free faces in pore fluid; once a critical stress is reached, the intergranular supporting 'neck' fails by plastic or brittle deformation, leading to compaction. Figure adapted from [60].
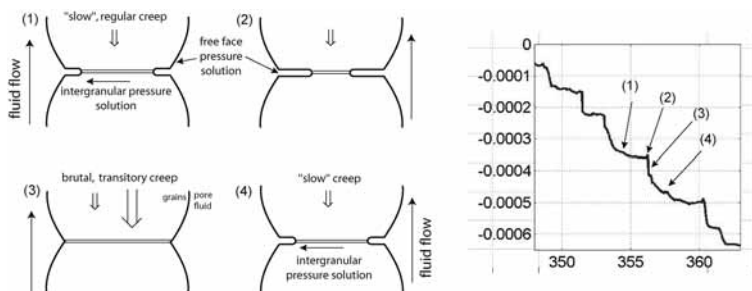


FIG. 12: Schematic illustration of the cyclical strain mechanism proposed in this study. (1) Dissolution occurs predominantly in pores spaces. "Thin fluid film" intergranular pressure solution (IPS) is responsible for measured compaction. (2) Undercutting of the supporting 'neck' region continues by dissolution, IPS remains active. (3) As the 'neck' diameter continuously decreases, a critical yield stress is reached, causing a short episode of rapid plastic or brittle compaction. (4) A new deformation cycle starts. This cyclical deformation is envisaged to occur at a sample scale. Figure modified from [60].